

Reconstructing the Mesozoic evolution of the Gulf of Mexico Basin: A new model incorporating optimised and focused lithospheric deformation

Satyam Pratap Singh¹, Sabin Zahirovic¹, Maria Seton¹, Nicky M Wright¹, Nicholas Atwood², Catherine Belgarde³, and Claire Mallard¹

¹University of Sydney

²BHP Metals Exploration - North America

³BHP Metals Exploration

November 30, 2023

Abstract

The Gulf of Mexico (GoM) is one of the most extensively studied offshore regions, but its Mesozoic evolution remains uncertain. The presence of a thick sedimentary cover and Jurassic salt poses challenges for geophysical imaging, hindering our understanding of the Mesozoic depositional history and crustal architecture evolution. Current tectonic models with rigid plates fail to capture key aspects of GoM evolution. This study introduces a new deformable plate model with optimised focused deformation designed to dynamically adjust stretching factors (SF) during rift evolution. Our model, which calculates crustal thickness and tectonic subsidence (TS) through time and accounts for stretching and thermal subsidence, can explain the depositional history of the pre-salt section and crustal architecture evolution of the GoM. Our model produces a predicted present-day crustal thickness with a root mean square error of 5.6 km with the GEMMA crustal thickness model. The resultant TS of ~ 1.5 km before the Yucatán block drifted, provides routes for the deposition of red beds through the paleo drainage systems of the northern GoM as successor basin infilling. The model explains ~ 40 Myrs of missing sedimentary strata, which we attribute to rapid subsidence in the central GoM, shifting red beds deposition beneath the Jurassic salt formations. Extension rate and SF calculations reveal a transition from a magma-rich to a hyperextended margin, with possible mantle exhumation. Our model can be useful in understanding the extent of other Jurassic deposits in the GoM basin and offers a robust framework for comprehending global passive rift margin evolution.

Hosted file

980130_0_art_file_11615534_s4h6jq.docx available at <https://authorea.com/users/703904/articles/689534-reconstructing-the-mesozoic-evolution-of-the-gulf-of-mexico-basin-a-new-model-incorporating-optimised-and-focused-lithospheric-deformation>

1
2 **Reconstructing the Mesozoic evolution of the Gulf of Mexico Basin: A new model**
3 **incorporating optimised and focused lithospheric deformation**
4

5 **Satyam Pratap Singh¹, Sabin Zahirovic¹, Maria Seton¹, Nicky M. Wright¹, Nicholas**
6 **Atwood², Catherine Belgarde², Claire Mallard¹**

7 ¹EarthByte Group, School of Geosciences, The University of Sydney, NSW 2006, Australia

8 ²BHP Metals Exploration, Tucson, Arizona 85704, USA

9
10 Corresponding author: Satyam Pratap Singh (satyampratap.singh@sydney.edu.au)
11

12 **Key Points:**

- 13
- 14 • A optimised deformable plate model for Gulf of Mexico (GoM) is introduced that
15 dynamically adjusts stretching factor during rift evolution.
 - 16 • The 40 Myrs gap in GoM's Mesozoic strata is due to rapid subsidence, shifting red bed
17 deposition beneath Jurassic salt formations.
 - 18 • The GoM basin transitioned from a magma-rich to a hyperextended margin with possible
19 mantle exhumation.

20 **Abstract**

21 The Gulf of Mexico (GoM) is one of the most extensively studied offshore regions, but its
22 Mesozoic evolution remains uncertain. The presence of a thick sedimentary cover and Jurassic
23 salt poses challenges for geophysical imaging, hindering our understanding of the Mesozoic
24 depositional history and crustal architecture evolution. Current tectonic models with rigid plates
25 fail to capture key aspects of GoM evolution. This study introduces a new deformable plate
26 model with optimised focused deformation designed to dynamically adjust stretching factors
27 (SF) during rift evolution. Our model, which calculates crustal thickness and tectonic subsidence
28 (TS) through time and accounts for stretching and thermal subsidence, can explain the
29 depositional history of the pre-salt section and crustal architecture evolution of the GoM. Our
30 model produces a predicted present-day crustal thickness with a root mean square error of 5.6 km
31 with the GEMMA crustal thickness model. The resultant TS of ~1.5 km before the Yucatán
32 block drifted, provides routes for the deposition of red beds through the paleo drainage systems
33 of the northern GoM as successor basin infilling. The model explains ~40 Myrs of missing
34 sedimentary strata, which we attribute to rapid subsidence in the central GoM, shifting red beds
35 deposition beneath the Jurassic salt formations. Extension rate and SF calculations reveal a
36 transition from a magma-rich to a hyperextended margin, with possible mantle exhumation. Our
37 model can be useful in understanding the extent of other Jurassic deposits in the GoM basin and
38 offers a robust framework for comprehending global passive rift margin evolution.
39

40 **Plain Language Summary**

41
42 Unveiling the Gulf of Mexico's (GoM) hidden Mesozoic history has been challenging due to its
43 thick sedimentary cover and Jurassic salt deposits. Existing models using rigid plates have fallen
44 short in explaining the GoM's evolution. In this study, we introduce a new approach - a
45 deformable plate model that dynamically adjusts for stretching factors during rift evolution. Our
46 model successfully explains the pre-salt sedimentary history and crustal architecture evolution of
47 the GoM. It predicts current crustal thickness with impressive accuracy. Our findings suggest
48 that before the Yucatán block shifted, about 1.5 km of tectonic subsidence occurred, allowing for
49 the deposition of red beds in the northern GoM. Our model also solves a mystery - the absence of
50 around 40 million years of sedimentary layers - by proposing rapid subsidence in the central
51 GoM, shifting red bed deposition beneath Jurassic salt formations. Calculations reveal a
52 transition from a magma-rich to a hyperextended margin, with potential mantle exhumation.
53 Importantly, our model provides a valuable tool for understanding Jurassic deposits in the GoM
54 and offers insights into global rift margin evolution.
55

56 **1 Introduction**

57
58 The Gulf of Mexico (GoM) is shrouded in thick sedimentary layers, which conceal its oldest
59 rocks and makes it challenging to trace its Mesozoic geological evolution (Filina et al., 2022).
60 While seismic reflection data provides a means of seeing through the cover, the availability of
61 these datasets for the region is limited, as much of it is proprietary. Furthermore, the complex
62 interplay between thick sedimentary layers and pervasive mobile salts makes it difficult to
63 conduct detailed seismic imaging and investigate the pre-salt structures (Christeson et al., 2014;
64 Eddy et al., 2014), further obscuring its Mesozoic tectonic history.
65

66 Based on the available geophysical and geological constraints, numerous tectonic models have
67 been proposed for the formation of the GoM. Although these models generally agree on the
68 broader framework for the GoM formation, including the initiation of rifting after the Ouachita-
69 Marathon orogeny (which formed from the collision of Laurentia with Gondwana) in the Late
70 Paleozoic era and the completion of seafloor spreading by the mid Early Cretaceous period, they
71 vary in several aspects (Escalona et al., 2021; Marton & Buffler, 1994; Minguez et al., 2020;
72 Pindell et al., 2021; Pindell & Kennan, 2009). These key differences include the interpretation of
73 Triassic red bed deposition, the timing of initiation of continental rifting, timing of salt
74 deposition in relation to oceanic crust formation, the mode of the breakup, and the pre-rift GoM
75 fit of the crustal blocks. For example, the conventional model for red bed formation suggests that
76 red bed deposition occurred in rifts and grabens during initial Pangea rifting during the Late
77 Triassic attributed to the existence of the South Georgia Rift (SGR) in eastern North America
78 (Figure 1; Salvador, 1991). However, such rift-graben structure is not pervasively observed in
79 seismic section across the GoM basin suggesting some alternative model for red bed deposition
80 (Filina et al., 2022; Milliken, 1988; Nicholas & Waddell, 1989; J. W. Snedden & Galloway,
81 2019). Further complicating the understanding of red bed deposition is the several millions of
82 years of hiatus in stratal deposition between the Triassic red beds and the overlying Jurassic
83 Louann salt (Filina et al., 2022; Marton & Buffler, 1994; Salvador, 1991). In a broader sense,
84 there are certain regions along the Yucatán margin and eastern GoM basin (Figure 1 and 2) that
85 exhibit pre-salt deposits, evident in seismic sections (Horn et al., 2016; O'Reilly et al., 2017;
86 Williams-Rojas et al., 2012). However, the precise model for their formation, and whether they
87 represent red bed deposits, remain uncertain due to the challenges posed by the thick
88 sedimentary cover impeding drilling efforts.

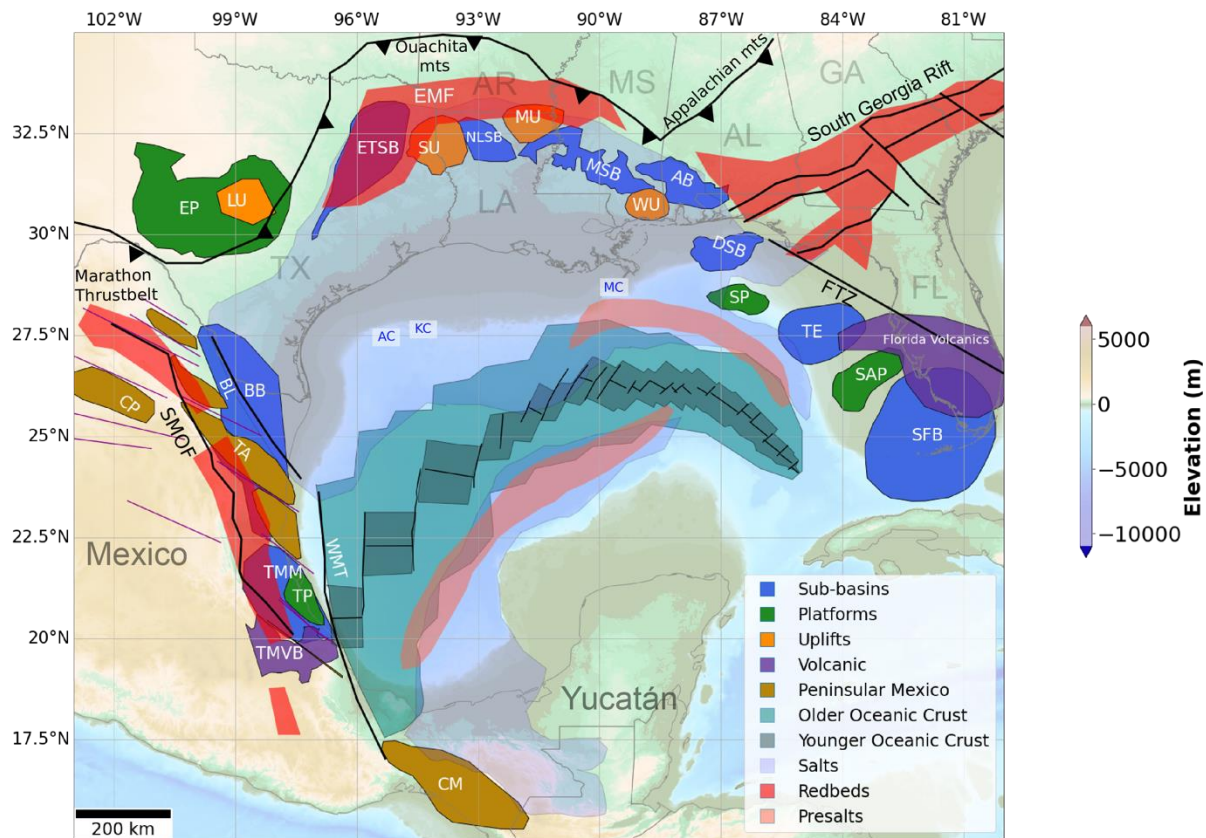
89
90 Gravity and seismic data indicate a significant portion of the GoM basin has a thinner crust than
91 typical continental crust, necessitating compensation to establish a closer fit between North and
92 South America before the breakup of Pangea (Christeson et al., 2014; Eddy et al., 2014; Filina,
93 2019). Based on these data, two plausible scenarios are postulated: either hyperextension and
94 mantle exhumation or the formation of thick oceanic crust preceding the primary opening of the
95 GOM during the Late Jurassic-Early Cretaceous (Filina & Beutel, 2022; Lundin & Doré, 2017;
96 Pindell et al., 2021). Moreover, seaward-dipping reflectors (SDRs), commonly associated with
97 magma-rich margins, have been observed in the seismic section of the eastern GoM (Filina et al.,
98 2022). Interestingly, seismic reflection data also reveals the presence of ridge-like basement
99 highs in the central to the northeastern half of the basin and at specific locations along the
100 northern Yucatán margin (Pindell et al., 2014). Notably, such ridge-like features are typically
101 associated with mantle exhumation and often related to magma-poor margins (Minguez et al.,
102 2020; Pindell et al., 2014). Consequently, the nature of rifting in the GoM, whether it leans
103 towards a magma-rich or magma-poor scenario, and the exact architecture of the crust formed
104 during seafloor spreading, including stretched continental crust, thicker oceanic crust, or
105 exhumed mantle, remain enigmatic.

106
107 The prevailing plate tectonic models for the opening of the GoM have predominantly employed
108 rigid plate assumptions (Filina & Beutel, 2022; Marton & Buffler, 1994; Minguez et al., 2020;
109 Pindell et al., 2021). However, a significant limitation of these models is their assumption that
110 the continental crust remained intact and undeformed during the opening of the basin, which
111 contradicts compelling geological and geophysical data from passive margins (Eddy et al., 2014,

112 2018; Minguetz et al., 2020; Rowan, 2014; Van Avendonk et al., 2015). In the GoM, seismic
 113 reflection and gravity interpretations offer insights into the significant amount of subsidence and
 114 deformation of the crust throughout its evolution, posing significant challenges to the rigid plate
 115 model (Filina et al., 2022; Pindell et al., 2014). Moreover, the presence of thin, high-velocity
 116 layers within the continental crust is believed to be remnants of the original pre-rift crust that
 117 experienced thinning and stretching during the opening of the GoM basin (Christeson et al.,
 118 2014; Eddy et al., 2014; Filina et al., 2022). These observations can only be adequately explained
 119 by adopting a deformable plate model that captures the deformation and evolution of the
 120 continental crust.

121
 122 Here we present a new deformable plate reconstruction model with an optimised focused
 123 deformation approach to reconstruct the Mesozoic history of the GoM. The core of our optimised
 124 focused deformation model lies in its ability to dynamically adjust the region between rigid
 125 blocks, accounting for the extent of thinning experienced during the rifting phase. This
 126 adjustment is meticulously tailored to exponentially increase the stretching factors seaward,
 127 ultimately leading to continental rupture and the formation of oceanic crust. Through our new
 128 approach, we aim to advance the understanding of the GoM's complex Mesozoic geological
 129 history, providing a comprehensive framework for interpreting its evolution and the key
 130 geological processes that have shaped the region.

131
 132
 133
 134



135

136 **Figure 1.** Tectonic elements in the GoM basin. Abbreviations: AB, Alabama basin; AC,
 137 Alaminos Canyon; BB, Burgos basin; BL, Burgos lineament; CM, Chiapas Massif; CP, Coahuila
 138 Platform; DSB, DeSoto salt basin; EP, Edwards platform; ETSB, East Texas salt basin; EMF,
 139 Eagle Mills Formation; FTZ, Florida Transfer Zone; KC, Keathley Canyon; LU, Llano uplift;
 140 MC, Mississippi Canyon; MSB, Mississippi basin; MU, Monroe uplift; NLSB, North Louisiana
 141 salt basin; SAP, Sarasota platform; SFB, South Florida basin; SMOF, Sierra Madre Oriental
 142 Fault; SP, Southern platform; SU, Sabine uplift; TA, Tamaulipas/San Carlos arch; TE, Tampa
 143 embayment; TMM, Tampico–Misantla–Magiscatzin; TMVB, Trans-Mexican Volcanic Belt; TP,
 144 Tuxpan platform; WU, Wiggins Uplift; WMT, Western Margin Transform. US States are
 145 abbreviated as TX, Texas; LA, Louisiana; AR, Arkansas; Ms, Mississippi; AL, Alabama and GA,
 146 Georgia. Figure modified after Snedden and Galloway (2019). Purple lines represent an en
 147 echelon fault array from Pindell et al. (2021) that influenced the motion of Peninsular Eastern
 148 Mexico during GoM rifting. CM and Oceanic Crust data are also from Pindell et al. (2021). The
 149 presalt basins are based on Filina et al. (2022).

150

151 **2 Geological History**

152

153 **2.1 Rifting Initiation and Early Magmatism**

154

155 During the Late Triassic period, the Yucatán region was connected to the North American plate,
 156 with its northern boundary marked by the Ouachita mountains and the western boundary
 157 demarcated by the Burgos lineament (BL) (Figure 1; Pindell et al., 2021; Snedden & Galloway,
 158 2019). Continental crustal extension commenced with rift development in eastern North America
 159 and back-arc rifting in Mexico (Izquierdo-Llavall et al., 2022; Pindell, 1985; Pindell et al., 2021).
 160 The exact timing of rift initiation is harder to constraint given the limited wells located in the
 161 northern GoM basin and Mexico. Nevertheless, most model suggests that the rifting started in
 162 Late Triassic (Escalona et al., 2021; Izquierdo-Llavall et al., 2022; Lundin & Doré, 2017; Pindell
 163 et al., 2021). This rift formation in eastern North America coincided with a period of intense
 164 magmatic activity known as the Central Atlantic Magmatic Province (CAMP). Large quantities
 165 of lava, dykes, and sills have been mapped, dating around 200 Ma marking a peak in CAMP
 166 magmatism (Marzoli et al., 2018). However, it is important to note that the extension between
 167 the Yucatán block and North America was relatively minor during this time, indicating a distinct
 168 tectonic behaviour compared to the rift development in other areas of the GoM (Kneller &
 169 Johnson, 2011; Pindell et al., 2021; Snedden & Galloway, 2019).

170

171 **2.2 Red bed deposition**

172

173 After the initiation of rifting and magmatism, the northern and eastmost regions of the GoM, as
 174 well as eastern Mexico, witnessed the deposition of distinctive sedimentary units comprising red
 175 to greenish-grey shales, white sandstones, and red dolomites, collectively forming the Eagle
 176 Mills Formation (Figure 1; Salvador, 1991; Snedden & Galloway, 2019). The age of the Eagle
 177 Mills Formation is considered to be Triassic (Carnian; 237–228.4 Ma) based on the discovery of
 178 a single-leaf fossil (*Macrotaeniopteris magnifolia*) in the Humble #1 Royston well (Arkansas,
 179 USA; Scott et al., 1961). Additional support for its Triassic age stems from fossil algae analysis
 180 (Horn et al., 2016; Williams-Rojas et al., 2012). To the west of the GoM basin, the Triassic

181 section in northeastern Mexico primarily consists of similar red beds, but with a relatively higher
182 proportion of volcanic rocks due to differing tectonic settings (Shann & Horbury, 2020).
183 Nevertheless, the precise dating of these rocks remains uncertain, and they are generally
184 considered Late Triassic to Early Jurassic in age (Cisneros & Lawton, 2011). Notably, these red
185 beds often exhibit interbedding with the CAMP lavas and sills (Frederick et al., 2020).

186
187 The significance of these Triassic deposits lies in their representation of the transitional phase
188 between the Paleozoic Ouachita-Marathon orogeny and the subsequent Mesozoic rifting, which
189 ultimately gave rise to the formation of the GoM. Traditionally, the prevailing model (Salvador,
190 1991) suggests that these red beds were deposited within grabens formed during the early stages
191 of Pangea rifting, primarily attributed to the presence of the Triassic South Georgia Rift (SGR) in
192 eastern North America (Figure 1). However, recent observations and a re-evaluation of older
193 seismic data have cast doubts on this conventional model. Seismic data from Arkansas,
194 Louisiana, and Texas reveal a lack of clear evidence for such extensive buried rift system in the
195 areas where the grabens were expected to be present (Milliken, 1988; Nicholas & Waddell, 1989;
196 Snedden & Galloway, 2019). Although, few basement fault like structures have been observed in
197 some seismic sections of northern GoM margin but they are not pervasive and very limited to
198 northern GoM (Frederick et al., 2020). Additionally, in north Texas, the Eagle Mills Formation
199 onlaps the deformed Paleozoic basement (Milliken, 1988), suggesting sediment infilling rather
200 than deposition in grabens. Moreover, recent seismic images demonstrate that the seismic
201 horizon of the base salt is predominantly unfaulted (Horn et al., 2016). Considering these
202 findings, an alternative model has emerged, proposing that the northern GoM experienced
203 minimal stretching during Late Triassic, and the red beds represent a successor basin deposit
204 resulting from the infilling of pre-existing accommodation created during the Ouachita-Marathon
205 orogeny (Snedden & Galloway, 2019). Moreover, the lithosphere may have thinned in a more
206 ductile manner after this minimal stretching phase (Pindell et al., 2021). This new perspective
207 challenges the traditional understanding of the GoM evolution and warrants further investigation
208 into the origin and depositional processes of the Late Triassic to Early Jurassic red beds.

209

210 **2.3 Pre-salt sedimentary basins**

211

212 The U-Pb analyses of well data from the northern GoM reveal that the youngest depositional age
213 of the red beds extended only until 205 Ma, followed by a significant hiatus until the deposition
214 of post-rift salt at 169 Ma (Dickinson et al., 2010; Umbarger, 2018; Wiley, 2017). The cause of
215 this missing stratal gap remains unknown. Intriguingly, multiple seismic surveys conducted in
216 the northern Yucatán margin, western and eastern GoM have identified thick pre-salt sediments,
217 indicating their presence in these regions (Horn et al., 2016; O'Reilly et al., 2017; van Avendonk
218 et al., 2015; Williams-Rojas et al., 2012). However, the western GoM presents challenges in
219 imaging through the extensive overlying salt (Horn et al., 2016; Williams-Rojas et al., 2012),
220 leading to ongoing debates regarding the existence of pre-salt sediments in this area. In the
221 northwestern part of the GoM basin along the GUMBO1 (Gulf of Mexico Basin Opening)
222 seismic profile (Figure 3), van Avendonk et al. (2015) proposed the presence of pre-salt
223 sediments based on P-wave velocities between 5 and 5.5 km/s (Figure 4). Conversely, Filina
224 (2019) offered alternative interpretations, considering potential fields, such as the presence of a
225 very thick salt layer or a "salt wall". Nevertheless, the Yucatán margin has been covered by
226 multiple seismic sections and modelled gravity and magnetic data supporting the existence of
227 pre-salt sedimentary layers, with estimated thicknesses ranging from 2 to 5 km (Figure 2, 4 and

228 5). Despite these observations, the precise formation processes of these pre-salt sediments remain
229 elusive due to the challenges associated with drilling through thick sedimentary layers.

230

231 **2.4 Rift-to-Drift transition and crustal extension**

232

233 The Yucatán block underwent a significant transformation during the Early and Middle Jurassic
234 period (~195 to ~170 Ma) as it transitioned from rift to drift, resulting in substantial stretching
235 and thinning of the continental crust. This process led to the development of a large region of
236 transitional crust (Figure 3, 4, and 5). Numerous models have been proposed to explain the rift-
237 to-drift transition in the GoM (Escalona & Yang, 2013; Filina et al., 2022; Minguez et al., 2020;
238 Pindell et al., 2021). Some suggest clockwise rotation of Yucatán (Freeland & Dietz, 1971),
239 while others propose anticlockwise rotation (Marton & Buffler, 1994; Minguez et al., 2020;
240 Pindell et al., 2021), and some even propose a southeast translation of the Yucatán block
241 (Anderson & Schmidt, 1983). However, with the availability of geophysical data, it is now well
242 understood that the Yucatán block underwent significant anticlockwise rotation. Paleomagnetic
243 data have revealed an approximate 60-degree rotation of the Chiapas Massif and Yucatán block
244 (Marton & Buffler, 1994). Seismic data has mapped fracture zones in the eastern GoM
245 (Christeson et al., 2014; Eddy et al., 2014), while gravity data has identified fracture zones and
246 Extinct Spreading Centres (Minguez et al., 2020). Aeromagnetic data has been used to map
247 seafloor rotational fabrics in the western and central GoM, revealing the presence of
248 anticlockwise rotation. However, precisely quantifying the amount of Yucatán rotation remains
249 challenging (Pindell et al., 2021).

250

251 On the easternmost side of the GoM basin (Figure 1), this rift-to-drift transition is associated
252 with various basement features, including the Florida Transfer Zone (FTZ; Marton & Buffler,
253 1994; Pindell et al., 2021; Pindell & Kennan, 2009). Evidence of increased Mesozoic extension
254 is observed through early Mesozoic volcanism in the area south of the FTZ (Figure 1). However,
255 the distribution of deformation during this transition remains poorly understood (Filina et al.,
256 2022; Pindell et al., 2021).

257

258 Crustal thickness estimates from the GUMBO seismic refraction experiment and GEMMA
259 crustal thickness model (Reguzzoni & Sampietro, 2015) reveal contrasting stretching patterns
260 between the eastern and western regions of the GoM (van Avendonk et al., 2015). The central
261 and western GoM region (Figure 3) exhibits distinctive extension characteristics. Unlike typical
262 rifted margins, which are usually less than 300 km wide (Harry et al., 2003), this region displays
263 an unusually broad area of highly extended crust spanning approximately 425 to 500 km in the
264 western and central GoM (Huerta & Harry, 2012). Conversely, the eastern portion of the North
265 American GoM margin is less than 250 km wide (Huerta & Harry, 2012). Moreover, the
266 northern GoM basin is marked by a series of elevated basement blocks associated with thick and
267 less extended continental crust, while deep basins containing thick salt accumulations are
268 interspersed between them, characterised by thinner and more extended continental crust
269 (Marton & Buffler, 1994). One prominent geological feature is the Sabine uplift, believed to
270 have formed as a mid-rift high during the opening of the GoM in the Triassic period (Adams,
271 2007). Geophysical data confirms the Sabine uplift as a block of thick crust, with deep wells
272 recovering late Paleozoic sediments and Mississippian volcanic rocks (Marton & Buffler, 1994).
273 These Mesozoic uplifted areas experienced subsequent phases of reactivation and further uplift

274 during the middle to late Cretaceous and Paleocene-Eocene (Adams, 2007). The shape and style
275 of these resulting uplifted areas were strongly influenced by pre-Jurassic northwest-southeast
276 transform fault lineaments. The variations in crustal stretching and the presence of elevated
277 blocks and deep basins in different regions of the GoM highlight the complex and heterogeneous
278 nature of the rift-to-drift transition, shedding light on the intricate processes involved in the
279 evolution of this dynamic basin.

280

281 **2.5 SDRs and magnetic anomalies formation**

282

283 Seismic data analysis in the northeastern and southern parts of the GoM basin, along the Yucatán
284 margin, has revealed the presence of basinward-dipping reflections known as SDRs (Eddy et al.,
285 2014; Hudec et al., 2013; Hudec & Norton, 2019; Williams-Rojas et al., 2012). These SDR
286 complexes exhibit significant deformation and are believed to have formed due to intense
287 magmatic activity, probably during the CAMP magmatism event (Filina et al., 2022). Notably,
288 these SDRs align with prominent magnetic anomalies in the region, suggesting a close
289 association with rift-related magmatism (Figure 2). The magnetic anomalies exhibit distinct
290 characteristics, such as long-wavelength, rounded, or oblate shapes. One particularly noteworthy
291 magnetic high running north-south off the western Yucatán shelf margin is referred to as the
292 Campeche magnetic anomaly (CMA). The CMA shares similarities in shape and intensity with
293 the prominent Houston magnetic anomalies (HMA) and Florida magnetic anomalies (FMA)
294 found along the northern continental margin of the GoM (Pindell et al., 2016). Potential field
295 modelling suggests that the CMA are likely associated with volcanic flows formed within the
296 syn-rift sections of rift basins (Pindell et al., 2016). However, due to their significant burial
297 depth, it remains challenging to determine whether they are indeed SDRs. A similar origin has
298 been proposed for the HMA (Mickus et al., 2009). Furthermore, the Yucatán magnetic anomaly
299 (YMA) in the southern GoM basin also coincides with interpreted SDRs observed in seismic
300 images (Filina et al., 2022; Steier & Mann, 2019). The identification of SDRs and their
301 association with magnetic anomalies provides crucial insights into the magmatic processes and
302 tectonic evolution of the GoM. These intriguing findings support the interpretation of the GoM
303 as a magma-rich margin.

304

305 **2.6. Salt deposition**

306

307 During the mid-Jurassic, basin-wide salt was deposited in the GoM, but there remains a debate
308 regarding the precise timing of salt deposition in relation to the onset of seafloor spreading
309 (Pindell et al., 2021; Salvador, 1991; Snedden et al., 2018). Initially, the age of the Louann salt
310 and associated anhydrites was assumed to be Callovian (~162 Ma) based on the age of the
311 overlying Norphlet Formation and Oxfordian Smackover Carbonate (Salvador, 1991). However,
312 strontium (Sr) isotopes suggest an older age of 169–170 Ma (Pindell et al., 2021). The deposition
313 of the such salt is believed to have occurred rapidly, taking less than a million years (Warren,
314 2006). This estimation finds support from numerical models of similar salt deposition in the
315 South Atlantic and stratigraphic analyses of the Santos Basin in Brazil (Montaron & Tapponnier,
316 2009). Moreover, present-day observed rates of salt deposition in known areas (see Davison et
317 al., 2012) align with the suggestion of rapid deposition in the GoM. Nevertheless, such rapid salt
318 deposition is only possible with rapid subsidence during salt deposition (Davison et al., 2012).
319 Some authors (Hudec et al., 2019; Pindell et al., 2021) propose an alternative interpretation,

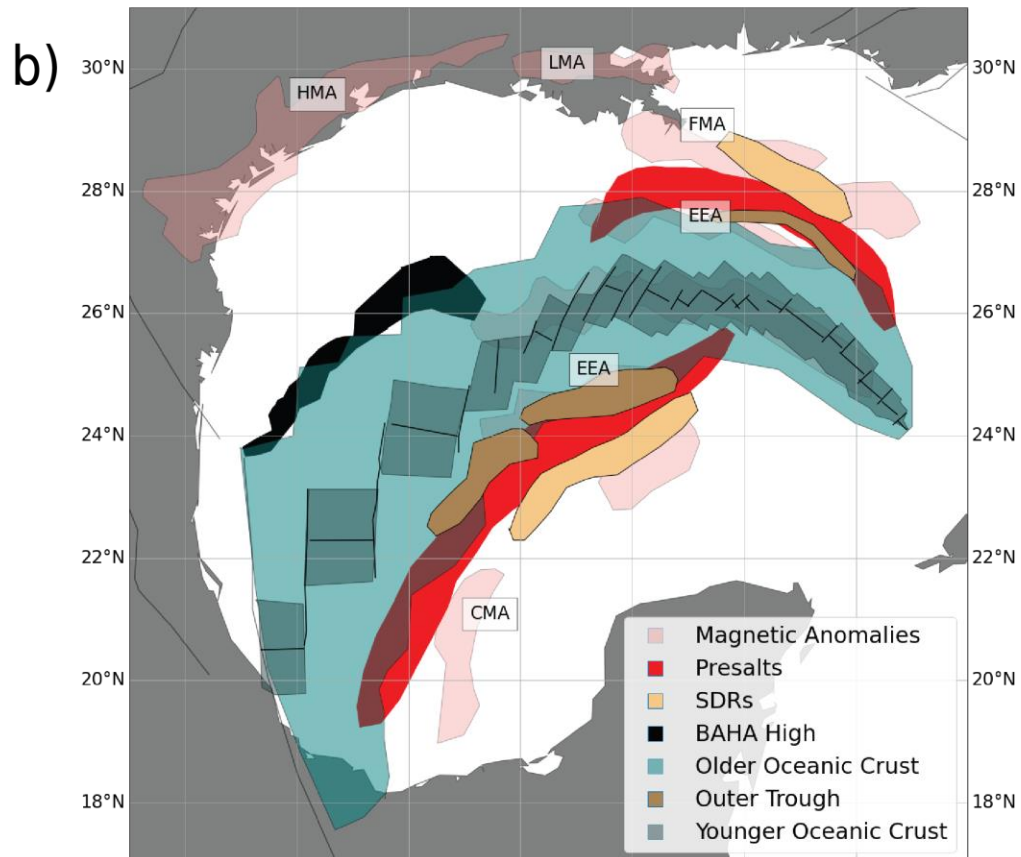
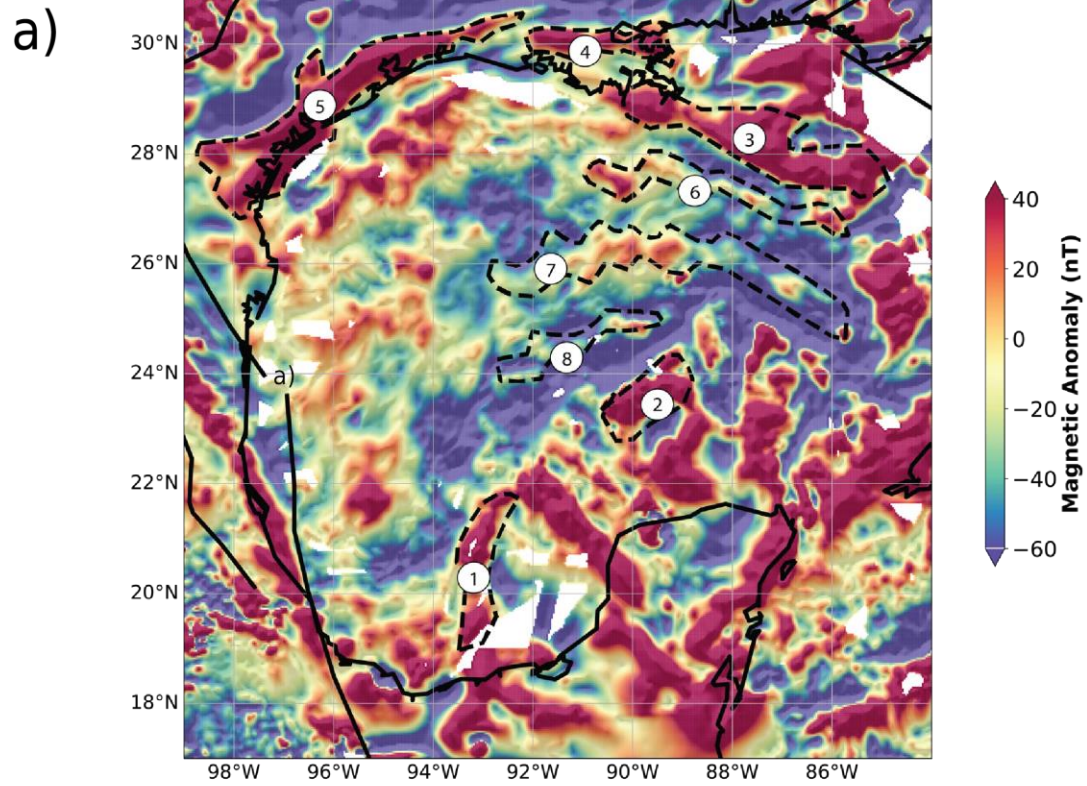
320 suggesting that the salt may not represent a syn-rift deposit, but rather could have been deposited
321 after the onset of oceanic spreading. This possibility is consistent with the absence of rift faults
322 in observed seismic horizons of salts from the GoM (Horn et al., 2016). Alternatively, it is
323 plausible that the salt deposition coincided with the onset of seafloor spreading (Lundin & Doré,
324 2017).

325 **2.7. Seafloor spreading**

326 The timing of seafloor spreading initiation and the nature of the crust beneath the salt layers in
327 the GoM have been the subject of extensive research and debate (Escalona et al., 2021; Marton
328 & Buffler, 1994; Minguez et al., 2020; Pindell, 1985; Pindell & Kennan, 2009). Various models
329 have been proposed, relying on seafloor spreading rates and geophysical observations to
330 determine the timing of seafloor spreading. For instance, satellite gravity data and the Extinct
331 Spreading Ridge magnetic anomaly (ESRA; Figure 2) have been used to constrain the rotation of
332 the Yucatán block with spreading rate estimations from the known East Coast magnetic anomaly
333 (ECMA) and Blake Spur magnetic anomaly (BSMA) in the Central Atlantic (Marton & Buffler,
334 1994; Pindell et al., 2021; Pindell & Kennan, 2009). The asymmetry in the crust's nature on
335 either side of the ESRA has led to different explanations. For example, Filina and Beutel (2022)
336 proposed two phases of seafloor spreading with ridge reorganisation in between each phase.
337 Similarly, Pindell et al. (2021) also suggested a two-phase spreading without ridge
338 reorganisation. Another hypothesis suggests that mantle exhumation in the northeastern region of
339 the GoM, followed by symmetrical oceanic spreading, could explain the asymmetry (Minguez et
340 al., 2020). Observations of minor magnetic anomalies called En Echelon anomalies (EEA) by
341 Minguez et al. (2020) align with the start of seafloor spreading, indicating some level of
342 symmetry in the GoM's structure during the breakup (Figure 2). However, these anomalies were
343 interpreted as a peridotite ridge rimming the oceanic crust rather than direct evidence of
344 spreading (Minguez et al., 2020). Additionally, seismic reflection data in the central to
345 northeastern GoM and along the Yucatán margin reveal ridge-like basement highs, interpreted as
346 a mechanical boundary between the crust and mantle, allowing for mantle exhumation (Minguez
347 et al., 2020; Pindell et al., 2014). These basement highs are bordered on the outside by the outer
348 trough, which exhibit a drop in basement height by ~2 km adjacent to the inferred oceanic crust
349 (Figure 2; Hudec et al., 2019). The trough and basement high are related to a regional magnetic
350 low and a set of EEA magnetic anomalies, respectively. The presence of ridge-like basement
351 high along with outer trough point to a magma-poor evolution of GoM. Continuation of these
352 EEA anomalies in the western region of the GoM is marked by the BAHA high, which exhibits 3
353 km of relief in seismic data, but the magnetic anomaly signature is not very clear. The BAHA
354 high has been interpreted to have formed at the same time as the deposition of salt, but the nature
355 of the crust is still debated (Hudec & Norton, 2019). Initial interpretations (Fiduk et al., 1999)
356 assumed it to be older oceanic crust formed during an early stage of spreading, while others
357 propose hyperextended continental crust or exhumed mantle (Pindell et al., 2021). Hudec et al.
358 (2019) proposed that the BAHA high might be a volcanic ridge that formed before seafloor
359 spreading but after the salt deposition (since salt onlaps onto the BAHA high).

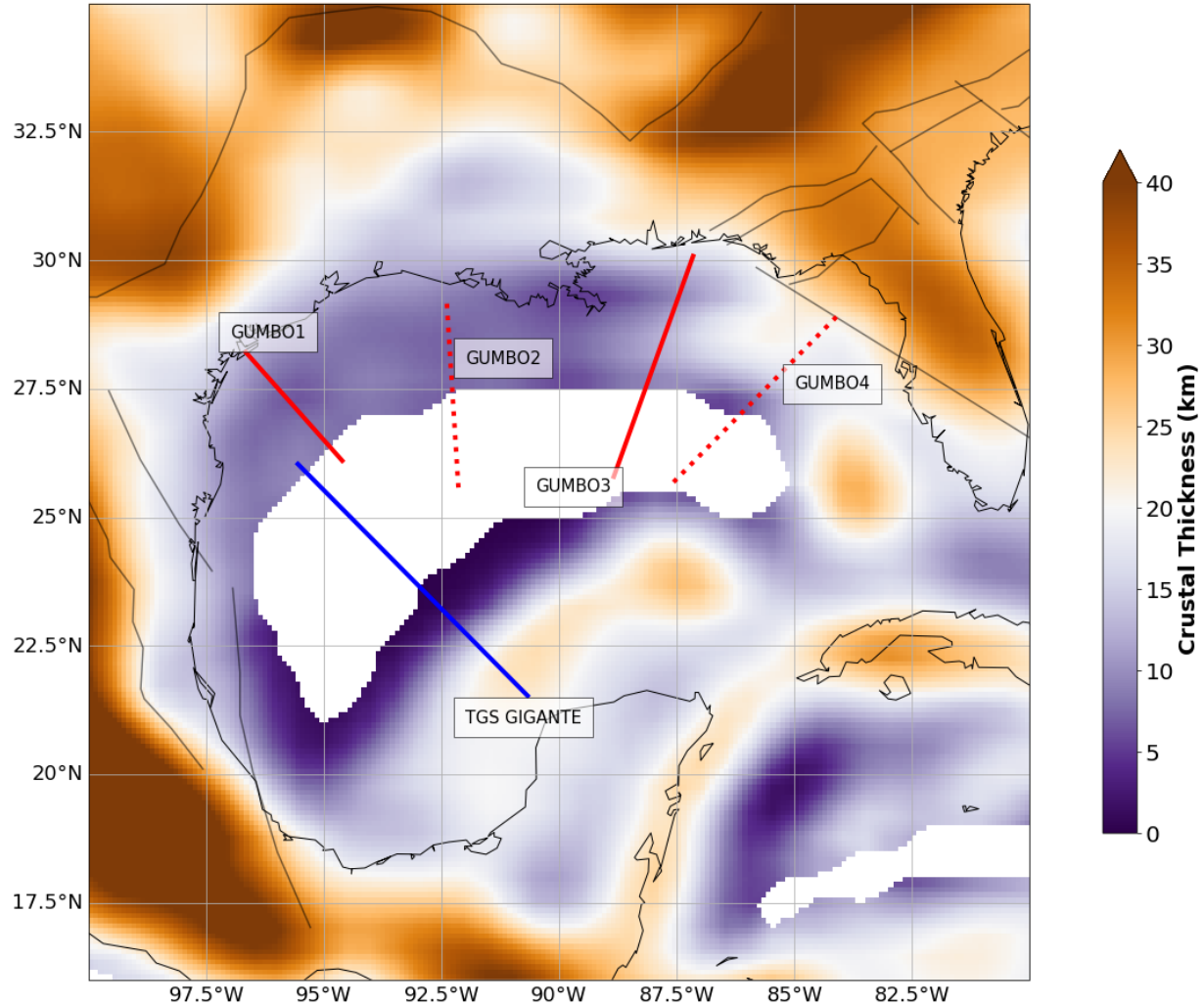
360 The GUMBO seismic imaging also revealed lateral variations in crustal composition across the
361 northern GoM and identified two distinct crustal zones within the oceanic domain (Figures 4 and
362 5). GUMBO3 led to an interpretation of a two-layered structure with a basaltic upper layer and a
363 gabbroic layer beneath, reaching a thickness of up to 9 km (Eddy et al., 2014). In contrast,

367 GUMBO4 imaged a thinner oceanic crust, around 5 km thick, with a uniform composition,
368 suggesting limited magma supply during its formation (Christeson et al., 2014; Minguez et al.,
369 2020). The presence of SDRs and coincident HMA, CMA, and other high magnetic anomalies
370 led to suggestion of a magma-rich nature of GoM evolution (Filina & Hartford, 2021) but on the
371 other hand presence of EEA, outer trough, and ridge-like basement high, points towards a
372 magma-poor origin of GoM (Minguez et al., 2020; Pindell et al. 2016).
373



375
376
377
378
379
380
381
382
383
384
385
386
387
388
389
390
391
392
393
394
395
396
397
398
399
400
401
402
403

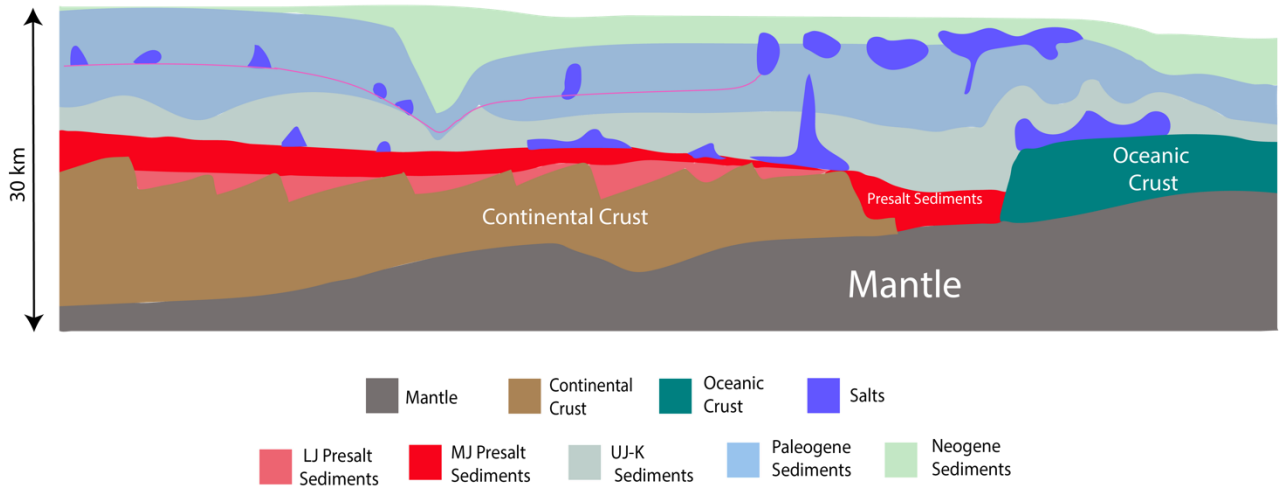
Figure 2. a) Magnetic anomaly map of the region (Meyer et al., 2017) showing important magnetic high (shaded black lines from Minguez et al., (2020) : (1) is the Campeche magnetic anomaly (CMA) (2) is the Yucatán magnetic anomaly (YMA) (3) is the Florida magnetic anomaly (FMA) (4) is the Louisiana magnetic anomaly (LMA) (5) is the Houston Magnetic Anomaly (HMA) 6) and 8) are En Echelon anomalies (EEA) and 7) is the Extinct Spreading Ridge Anomaly (ESRA). b) An illustration of the important geophysical interpretations in the region compiled from different sources. The presence of SDRs aligning with significant magnetic anomalies suggests a strong association with rift-related magmatism in the eastern GoM. The HMA, LMA, and CMA all are characterised by similar long-wavelength, rounded, or oblate-shaped anomaly pattern. The HMA and CMA likely indicate volcanic flows formed within the syn-rift sections of rift basins (Mickus et al., 2009), although confirming their nature is challenging due to their considerable burial depth. Notably, these anomalies and SDRs are not located at the transition to the oceanic crust. Another magnetic feature called EEA consists of smaller magnetic highs. Based on analog rock properties modelling, the EEA suggests the existence of a narrower zone of exhumed serpentinised mantle along the eastern GoM (Minguez et al., 2020). Seismic reflection data have revealed presence of ridge-like basement highs, interpreted as a mechanical boundary between the crust and mantle, facilitating mantle exhumation (Minguez et al., 2020; Pindell et al., 2014). These basement highs correlates well with the set of EEA magnetic anomalies. Moreover, these basement highs are bordered by the outer trough, which exhibits a deepening of the basement by 2 km adjacent to the inferred oceanic crust. BAHA high located in western GoM indicates a relief of 3 km in seismic data, the magnetic anomaly signature is less distinct here. The origin of the BAHA high is still debated, with some initial interpretations suggesting it to be older oceanic crust formed during an early stage of spreading, while others propose hyperextended continental crust or exhumed mantle (Hudec & Norton, 2019; Pindell et al., 2021; Hudec et al., 2019). The older and younger oceanic crust interpretation is based on Pindell et al. (2021)



404
 405
 406
 407
 408
 409

Figure 3. GEMMA crustal thickness model (Reguzzoni & Sampietro, 2015). The profiles marking the GUMBO experiments referred to in this study are depicted as red solid and dashed lines (Christeson et al., 2014; Eddy et al., 2018, 2018; Van Avendonk et al., 2015). GUMBO1 lies along western GoM while GUMBO3 and GUMBO4 is along eastern GoM. GUMBO2 lies in central GoM. The TGS GIGANTE line from Filina & Beutel (2022) is depicted as a blue line.

410
411



412
413
414
415
416
417
418
419
420
421

Figure 4. GUMBO1 line interpretation derived from Van Avendonk et al. (2015). The western GoM has a hyperextended continental crust with possible exhumation. Van Avendonk et al. (2015) interpreted high-velocity structure beneath the salt as pre-salt sedimentary deposits along western GoM. However, the presence of salt makes it difficult to perform detailed seismic imaging. An alternative interpretation of possible “salt wall” instead of these red beds is presented by Filina (2019).

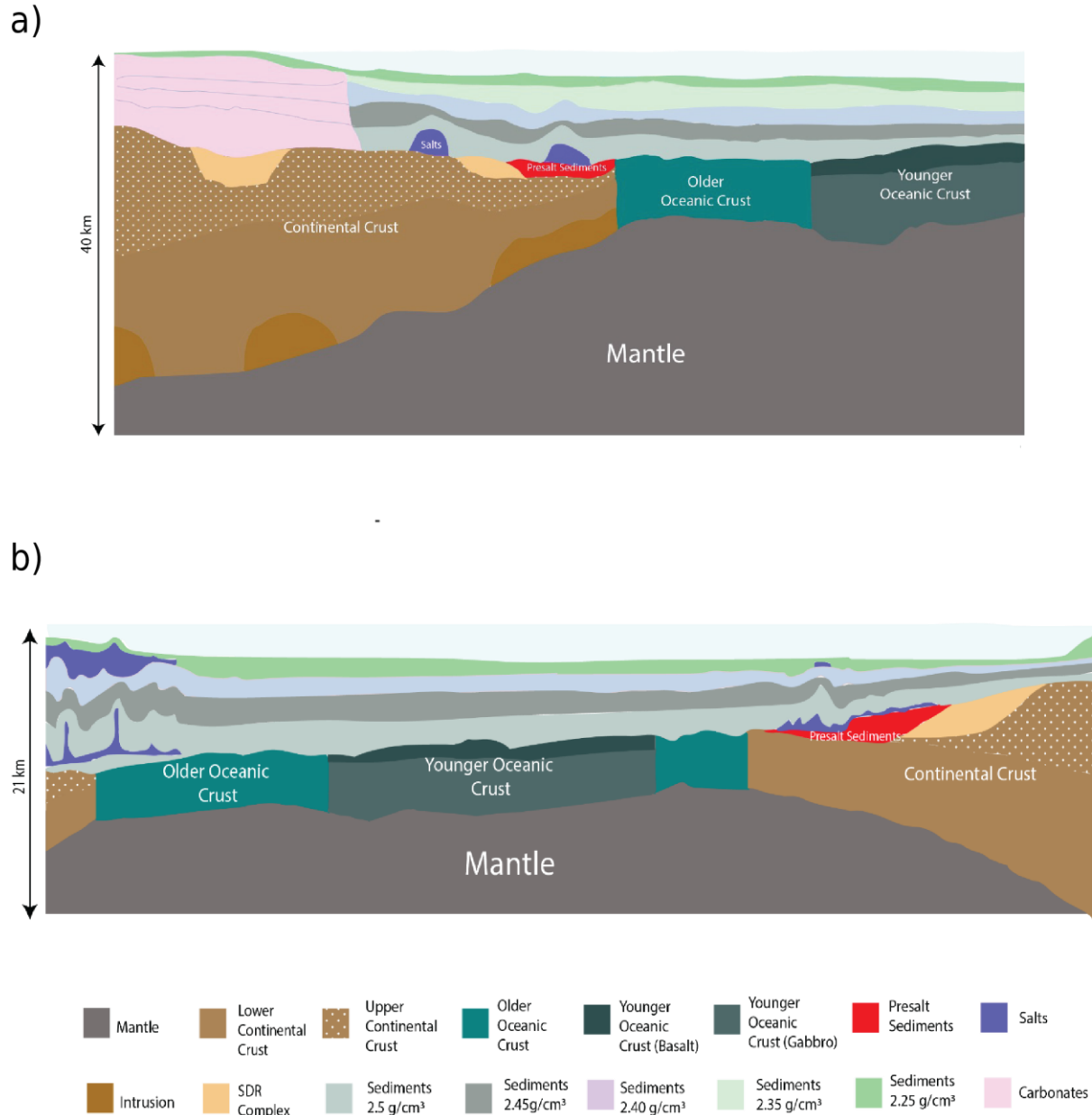


Figure 5. a) GUMBO3 line, and b) TGS GIGANTE line interpretations taken from Filina & Beutel (2022).

The Mesozoic geological history of the GoM poses significant challenges in tectonic reconstructions, demanding a comprehensive understanding of a range of complex factors. The large region of extensional deformation that has shaped the GoM necessitates a fresh approach to reconstructing the region. By addressing these challenges and adopting a comprehensive approach, one that incorporates a focused deformation approach, we can advance our understanding of the complex processes that have shaped the GoM and contribute to refining the tectonic reconstruction of this region.

3 Methodology

Traditional numerical approaches in plate tectonic reconstructions primarily focused on rigid plate motions, often neglecting the deformation of the plates themselves (Boschman et al., 2014; Müller et al., 2016; Pindell et al., 2021; Pindell & Kennan, 2009; Seton et al., 2012). However, a more recent global plate tectonic reconstruction model has emerged, introducing a novel methodology that incorporates deforming regions at plate boundaries through the establishment of deforming topology networks (Müller et al., 2019). To implement this approach, the deforming network is discretised into constant strain rate spherical triangular elements, utilising the Delaunay triangulation technique (Gurnis et al., 2018). By expressing the relative motion and velocities of the triangulation nodes within the deforming areas as finite rotations it becomes possible to calculate the strain rate associated with deformation at plate boundaries (Müller et al., 2019).

$$\dot{S} = \nabla \cdot \vec{u} = \dot{\epsilon}_D \quad (1)$$

\dot{S} is the strain rate; \vec{u} is the velocity of points and $\dot{\epsilon}_D$ is the dilatation strain rate.

Furthermore, this methodology allows for the estimation of the finite strain history of points within these deformation zones, enabling the calculation of crustal thickness over time. By employing the governing equations, the temporal variations in crustal thickness can be utilised to derive the tectonic subsidence of passive rift margins. This integrated approach provides a more comprehensive understanding of the dynamic passive rift evolution.

3.1 Modelling Crustal Thickness

The evolution of passive rift margins hinges upon the process of crustal thinning. By considering the incompressibility of the lithospheric block, the mass conservation equation can be employed to depict the time-dependent evolution of crustal thickness. This assumes that there is no net mass generation or loss during the deformation process, with horizontal divergence or convergence governing the vertical thinning or thickening (Gurnis et al., 2018; Müller et al., 2019). Hence, the crustal thickness at any time t can be calculated using equation 2.

$$\frac{DH}{Dt} = -H \cdot \dot{S} \quad (2)$$

where H is the crustal thickness and \dot{S} is the strain rate.

3.2 Modelling Tectonic Subsidence

Basin formation arises from the stretching of the continental lithosphere and is part of a broader continuum encompassing continental rifting, passive margin development, and the emergence of

483 a new oceanic crust (Brune et al., 2023; Şengör & Natal'in, 2001). Over geological timescales,
 484 the process of rifting culminates in the thinning and formation of passive margins, with seafloor
 485 spreading commonly commencing when the stretching factor (β) surpasses a critical threshold
 486 (Le Pichon & Sibuet, 1981). The β can be expressed as:

$$487 \beta = \frac{H_i}{H} \quad (3)$$

488 where H_i and H are the initial crustal thickness and crustal thickness at time t , respectively.

489 The isostatic adjustments stemming from lithospheric processes triggered by such stretching are
 490 reflected in subsidence histories, which offer insights into the mechanisms driving basin
 491 formation. Under the assumption of local isostatic equilibrium, the evolution of passive
 492 continental margins can be elucidated by McKenzie's (1978) stretching model. According to this
 493 model, the present-day depth of the seafloor at any point within a rift is contingent upon the
 494 timing and duration of rifting, the elapsed time since rifting cessation, and the stretching factor
 495 (β). Nevertheless, stretching alone does not govern tectonic subsidence (McKenzie, 1978).
 496 Subsidence analysis of most passive rift margins worldwide reveals that subsidence occurs
 497 through a combination of mechanisms. Initially, subsidence arises from rifting and extension of
 498 the continental crust and also due thermal anomaly from upwelling of asthenosphere. After the
 499 stretching ceases subsidence it is characterised by a slower diffusive decay of thermal anomaly
 500 which will further produce a thermal subsidence attributable to the gradual cooling and
 501 rethickening of the stretched lithosphere (Jarvis & McKenzie, 1980).

502 For our model, the subsidence due to the extension (TS_1) can be calculated using the thinning
 503 factor.

$$504 TS_1 = A \left(1 - \frac{1}{\beta} \right) \quad (4)$$

505 However, the loss of heat and thermal subsidence actually commences during the extension
 506 phase and needs to be considered simultaneously to obtain a realistic estimate of syn-rift
 507 extension (Jarvis & McKenzie, 1980). Therefore, slow thermal subsidence (TS_2) can be
 508 calculated by estimating temperature evolution using the advection-diffusion equation 6.

$$509 TS_2 = B \int_0^{L_c} (T'(z) - T(z)) \quad (5)$$

528 where T' and T are steady state (equation 6) and initial temperature, L_c is the thickness of the
 529 lithosphere, and z is the depth from the surface.

530

$$531 \quad \frac{dT}{dt} = \kappa \frac{d^2T}{dz^2} - v(z) \frac{dT}{dz} \quad (6)$$

532

533

534 The thermal diffusivity κ represents how heat spreads in a material. The vertical velocity,
 535 denoted as $v(z)$, arises from stretching effects. At the top surface (where $z=0$), the vertical
 536 velocity is zero. At the bottom surface (where $z=L_c$), it is represented as $-V_0$ and varies linearly
 537 with depth (z).

538 A and B are constant ratios that depend on the density of crust (ρ_c), mantle (ρ_m), asthenosphere
 539 (ρ_a), and thermal expansion coefficient (α) and calculated as follows

540

$$541 \quad A = \frac{(\rho_m - \rho_c)}{(\rho_a - \rho_w)} L_c \quad (7)$$

542

543

$$544 \quad B = \frac{\alpha \rho_m}{(\rho_a - \rho_m)} \quad (8)$$

545

546

547 It is worth noting that our subsidence model does not account for factors such as sediment
 548 accumulation and loading, orogenic loading, salt tectonics or subsidence due to dynamic
 549 topography.

550

551 **3.3. Focused Deformation**

552

553 Conventional models for crustal stretching typically assume uniform thinning and constant strain
 554 throughout the deformable zone when calculating crustal thickness and tectonic subsidence
 555 (Müller et al., 2019). However, this assumption does not hold true in many geological scenarios.
 556 Asymmetric subsidence patterns are commonly observed in basins during the rifting and breakup
 557 phase, resulting in enhanced subsidence towards the seaward side of the hinge zone (Huerta &
 558 Harry, 2012; Xie & Heller, 2009). This is because of focused extensional strain distribution,
 559 which can be attributed to brittle and ductile weakening processes (Brune et al., 2023). For
 560 instance, lithospheric “necking” can cause localised thinning by a large-scale thermal weakening
 561 process that transforms the originally cold and strong lithosphere into a hotter and weaker mantle
 562 (Chenin et al., 2018). Variations in crustal strength and viscosity can also lead to uneven
 563 deformation, resulting in focused zones of deformation (Bott, 1992; Ebinger et al., 2017). To
 564 accurately capture these complexities, numerical models incorporating non-uniform thinning and
 565 variable strain distributions are necessary. To address this, a modified extension model based on
 566 Jarvis & McKenzie, (1980) can be employed to calculate the tectonic subsidence of the passive
 567 margin during initial rifting, integrating the concept of focused deformation within the deforming
 568 plate motion model (Figure 6a).

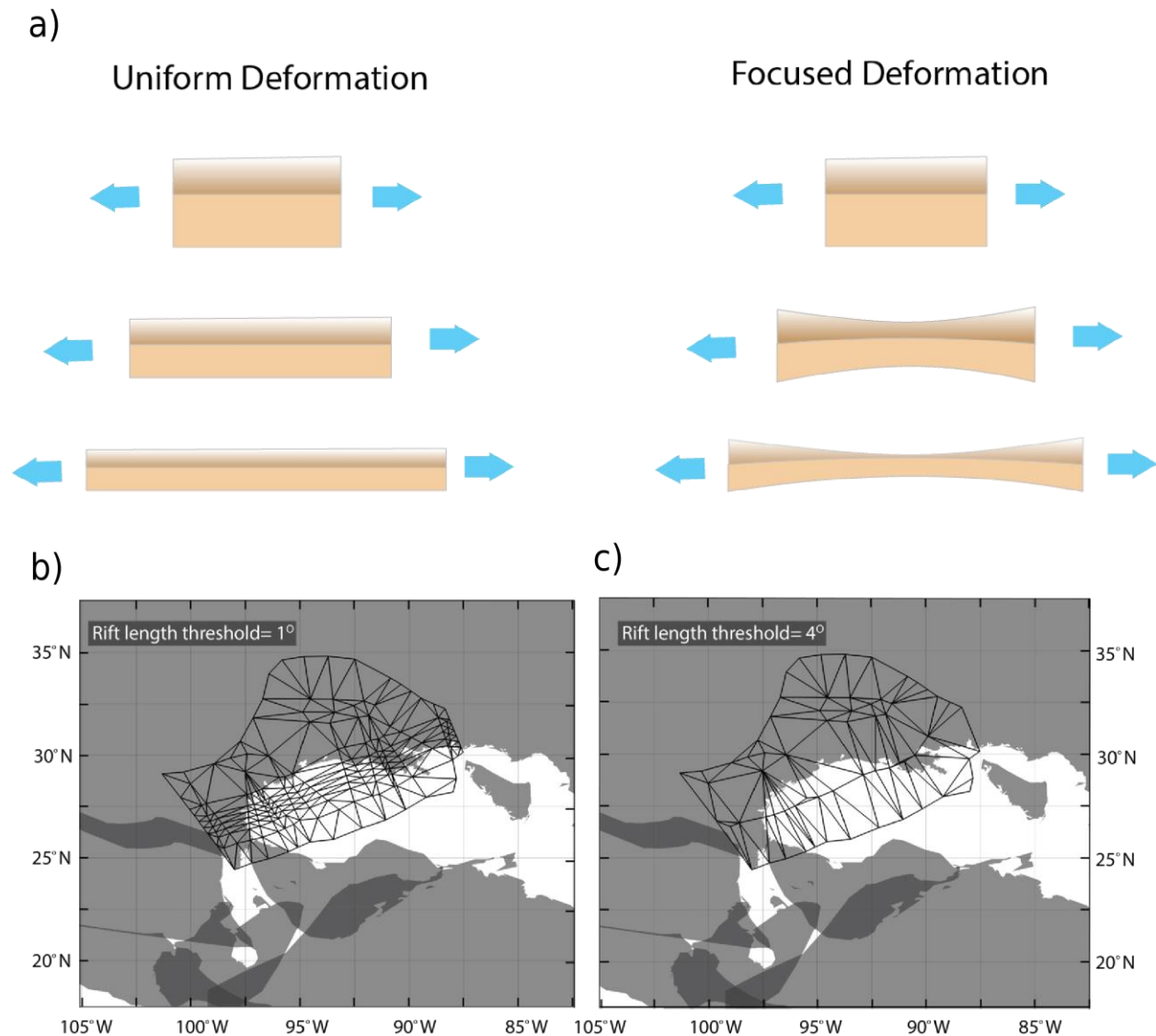
569 In the focused deformation model, stretching factors evolve over time, initially exhibiting a more
 570 uniform distribution and exponentially increasing seaward until continental rupture and oceanic

571 crust formation occurs. Our method allows for the control of the spatial variation of strain rate in
572 a rift profile by varying the **exponential stretching coefficient** (C) parameter while ensuring that
573 the network triangulation is sub-divided to fit the exponential curve within a certain tolerance
574 specified by the rift strain rate resolution and rift edge length threshold. The rift strain rate
575 resolution parameter is used to determine when rift edges in network triangulation need to be
576 subdivided to match the exponential curve within a certain tolerance. However, the sub-division
577 is also limited by the rift edge length parameter, which specifies the minimum length (in degrees)
578 of the rift edges that will not be further subdivided, controlling the spatial variation of strain rate
579 perpendicular to the rift profile (Figure 6b and 6c). The strain rate along the rift profile can be
580 represented as:

$$\dot{\epsilon}(x) = \dot{\epsilon}_0 \cdot e^{cx} \cdot \frac{c}{(e^c - 1)} \quad (9)$$

584 where $\dot{\epsilon}_0$ is undivided strain rate, c is the exponential stretching coefficient, and x is normalised
585 distance which is 0 at the unstretched point and 1 at the stretched point.
586
587

588



589

590

591

592 **Figure 6.** a) Model showing the difference between uniform and focused deformation where the593 top layer represents the crust, and the bottom layer represents the lithospheric mantle. **b-c)**

594 Deformation topology network (black mesh) used in this study and comparison of parameters

595 showing how rift length threshold is used to divide the strain rate in the deformation mesh. The

596 figure (b) has a rift length threshold value of 1.0, while (c), have a rift length threshold value of

597 4.0. The **strain rate resolution** parameter guides the decision on when to subdivide the network

598 (in perpendicular to the rift direction) to match the exponential curve within a certain tolerance,

599 hence controlling the strain rate perpendicular to the rift. The **rift edge length threshold**

600 parameter further controls the division of the topological network. The minimum possible

601 element length of topological network cannot be less than this parameter, thereby governing the

602 non-uniform spatial variation of strain rate. Grey blocks refer to rigid continental block, which

603 overlaps in the regions of tighter pre-Pangea fit which have also undergone deformation.

604 However, these regions are out of scope for this study.

605
 606
 607
 608
 609
 610
 611
 612
 613
 614
 615
 616
 617
 618
 619
 620
 621
 622
 623
 624
 625
 626
 627
 628
 629
 630
 631
 632
 633
 634
 635
 636
 637
 638
 639
 640
 641
 642
 643
 644
 645
 646

3.4 Optimising the Model

Our numerical model relies on a set of initial conditions and model parameters (Table 1) that must be determined to reconstruct the stretching factor, crustal thickness, and tectonic subsidence history. Of utmost importance are the deformation topology network between the Yucatán and North America blocks, which defines the extension region, and the relative plate motions between the blocks, which serves as the primary input variables for our model.

To create a deforming plate reconstruction, it is necessary to delineate the boundaries between the deforming and rigid areas (Figure 6b & c; Müller et al., 2019). This requires thorough geological and regional investigations to ascertain the extent of the deformation zone in the geological past, which ultimately influences the overall distribution of strain rates at the plate boundaries. Considering that the motion between the Yucatán and North America blocks drives GoM tectonics, we constructed the deformable plate model utilising these blocks only (Marton & Boffler, 1994). While deformation in Mexico and Florida was active during the syn-rift phase (Pindell et al., 2021), we focused the deformation mesh on the GoM Basin treating Mexico and Florida as rigid blocks. The eastern boundary of our deforming zone is defined by the Burgos Lineament and Western Transform margin (Figure 1). The southern boundary is demarcated by the Yucatán block; however, in our reconstruction, the Chiapas block was not part of Yucatán until the Valanginian times (Pindell et al., 2021). The northern limit of our deformation zone is determined by the Ouachita-Marathon thrust belt and Triassic mid-rift high (Dickinson et al., 2010; J. W. Snedden & Galloway, 2019). Estimating the precise shape and location of the mid-rift high in the Triassic is challenging, but it can be inferred from the present-day Sabine Uplift, the primary GoM rift basin, and the deposition pattern of the Louann salt (Salvador, 1991; J. W. Snedden & Galloway, 2019). In our reconstruction, we introduced fixed non-deforming nodes around the Sabine Uplift to encompass this region. Furthermore, we finely tuned the fixed non-deforming nodes around these areas by matching the calculated crustal thickness from our model with known estimates from the GEMMA model (Reguzzoni & Sampietro, 2015).

Table 1. Parameters used in this study in generating our optimised deforming model. The crustal density values are derived from density calculations of GUMBO1 and GUMBO2, as detailed in Filina (2019). The density of water is referenced from Smith & Sandwell (1997), while the mantle density is taken from Zoback & Mooney (2010). For the purposes of this study, a standard lithospheric thickness of 125 km is assumed, in accordance with the thickness estimate derived from the shear wave velocity model within the unextended region (131 ± 28 km; Ho et al., 2016). It is worth noting that the lithospheric thickness within the GoM region exhibits variability in the present day. This variability is reflected in estimated thicknesses of 87 km in the oceanic domain and greater than 100 km in the northern GoM which due to extension and cooling (Nguyen et al., 2022).

Parameters	Values
Initial Crustal Thickness (H_i)	Constant for optimizing
Lithospheric Thickness (L_c)	125 Km
Density of Crust (ρ_c)	2800 kg/m ³

Density of Mantle (ρ_m)	3330 kg/m ³
Density of water (ρ_w)	1030 kg/m ³
Exponent Stretching Factor (C)	Constant for optimizing
Rift Length Threshold	Constant for optimizing
Strain Rate Resolution	Constant for optimizing
Thermal Expansion coefficient (α)	3.28e-5 °C ⁻¹
Thermal Diffusivity	8.04e-7 m ² /s

647
648 A second crucial input for our reconstruction is the relative plate motion between North America
649 and Yucatán. Various regional and global plate models can be employed, and their results can be
650 compared to recent observations (Boschman et al., 2014; Müller et al., 2019; Pindell & Kennan,
651 2009; Seton et al., 2012). We adopted Kneller and Johnson's (2011) plate reconstruction model,
652 which proposes a close fit of North America and Yucatán plate to restore the original position of
653 Yucatán prior to the rift-to-drift transition at ~195 Ma. This plate reconstruction model is based
654 on the restoration of crustal thickness and refraction lines. To model the rift-to-drift transition,
655 we assessed the flowlines generated by three different plate reconstruction models (Table 2).
656 Each model offers distinct interpretations of the history and processes that contributed to the
657 formation of the GoM (Table 1). Pindell et al. (2021), based on proprietary magnetic data,
658 propose one stage of continental rifting and two phases of oceanic spreading. It suggests a syn-
659 drift change in the position of the pole of rotation approximately 150 Ma and includes a potential
660 episode of mantle exhumation. Minguez et al. (2020) utilises gravity data to derive plate motions
661 and magnetic data to determine the timing and location of seafloor spreading. According to this
662 model, the GoM opened as a rift between South and North America, with seafloor spreading
663 commencing in the west and propagating eastward, concluding around 154 Ma. The Filina and
664 Beutel (2022) model, which integrates potential fields and seismic data, also proposes two
665 phases of oceanic spreading, with ridge propagation occurring approximately 151 Ma. Pre-drift
666 positions of the Yucatán block are defined using SDRs. This model suggests temporal variability
667 in the magmatic regime during GoM opening, ranging from CAMP (~200 Ma) to initial
668 amagmatic ultra-slow spreading (~165 Ma) followed by a faster magmatic phase of spreading
669 (~152 Ma). We compared the flowlines of these three models using the vertical gravity gradient
670 (VGG) grids data (Sandwell et al., 2021) based on two visible curvilinear rotation fabrics and an
671 extinct spreading centre. Based on closer match of these curvilinear rotation fabrics with
672 flowlines generated by Pindell et al. (2021) model, we selected it to be the most suitable input
673 model for our reconstruction.

674
675
676
677
678
679
680
681
682
683

Table 2. Summary of the models assessed in this study, documenting the timing, opening phase, and constraints used.

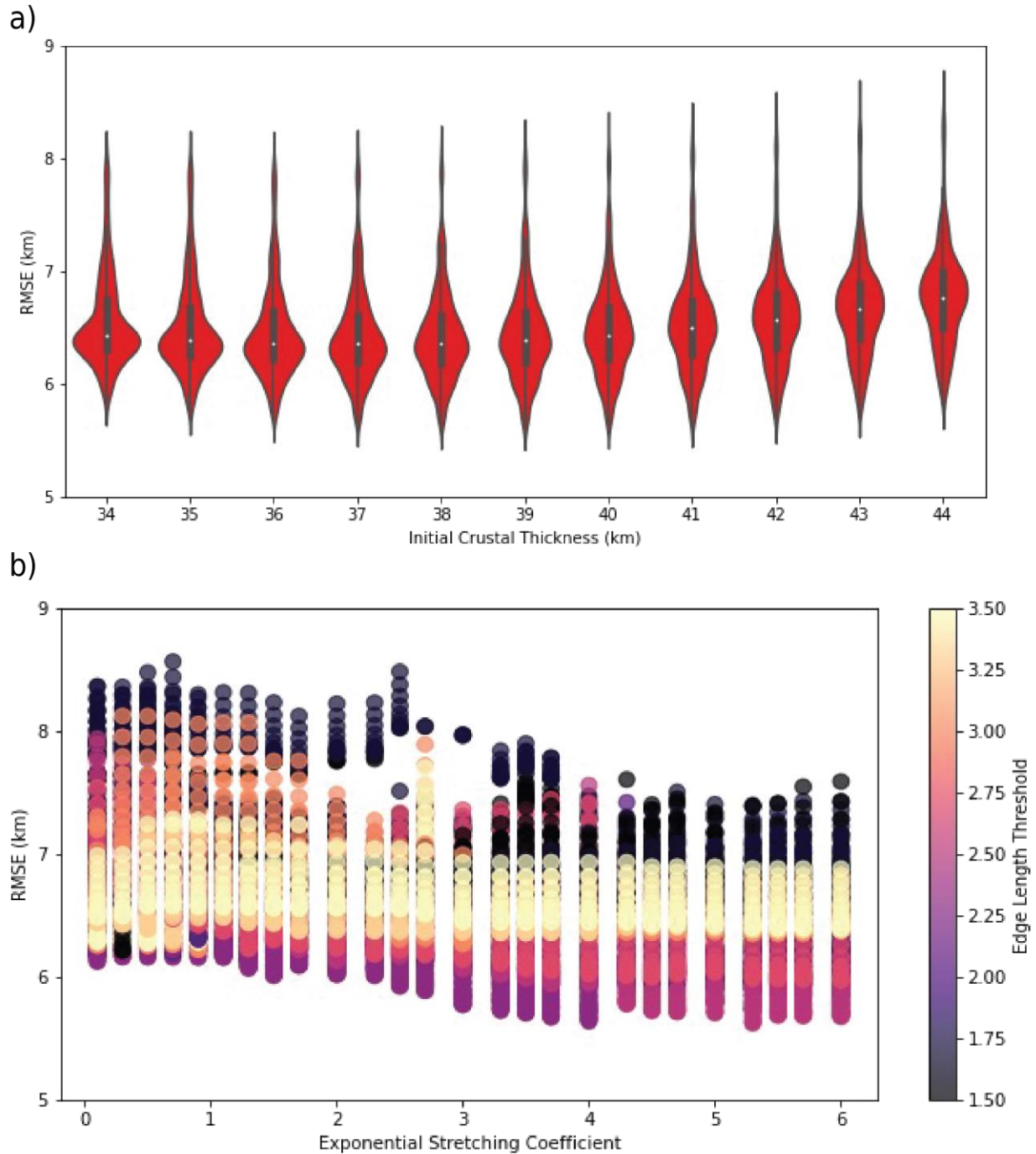
Model	Timing	Comments

Pindell et al. (2021)	195–167 Ma	Reconstruction: Start of the rift to drift transition. Constraints: CMA and HMA will be parallel to each other
	169 Ma	Reconstruction: Deposition of salt (based on recent Sr-isotope data)
	167–147 Ma	Reconstruction: The first phase of seafloor spreading. Constraints: The northern and southern anomaly trends (NMAT and SMAT) are interpreted as a transition between the exhumed mantle and oceanic crust.
	147–137 Ma	Reconstruction: The second phase of seafloor spreading. Constraints: Central magnetic anomaly trend (CMAT) interpreted as the youngest oceanic crust
Minguez et al. (2020)	203–169 Ma	Reconstruction: Syn-rift Phase Constraints: Subparallel opening to the South America plate
	170 Ma	Reconstruction: Deposition of salt
	169–166 Ma	Reconstruction: Exhumation of the mantle. Constraints: EEA and its conjugate are collinear.
	166–154 Ma	Reconstruction: Seafloor spreading. Constraints: ESRA can be produced by full spreading rate of 2.4 cm/year with Chron M2n at the extinct spreading center.
Filina and Beutel (2022)	220–169 Ma	Reconstruction: Syn-rift Phase. Constraints: SDRs on the Yucatán and North American margins should be near each other.
	169 Ma	Reconstruction: Deposition of salt
	169–165 Ma	Reconstruction: Post-continental stretching Constraints: Presence of Outer Trough on the northern Yucatán margin
	165–152 Ma	Reconstruction: First spreading phase Constraints: Thin and uniform oceanic crust

	152–135 Ma	Reconstruction: Second spreading phase Thick and layered oceanic crust
--	------------	--

684
685

686 In our approach, we employ pyGPlates (www.gplates.org) to forward model the evolution of
687 crustal thickness up to the present day, utilising the plate rotation and deforming topological
688 network as primary inputs. To ensure the accuracy of our model, we compare the calculated
689 crustal thickness at 0 Ma (present day) with the present-day crustal thickness estimates from
690 known GEMMA crustal thickness model (Reguzzoni & Sampietro, 2015). This comparison
691 allows us to search for optimal values of key parameters, including the edge length threshold,
692 strain rate resolution, and exponential stretching factor used for the distribution of strain rates in
693 passive rift margins. By achieving the closest match with the present-day crustal thickness, we
694 can identify the most suitable values for these parameters and enhance the reliability of our
695 reconstruction. Yet another critical input parameter for modelling the evolution of crustal
696 thickness over time is the initial crustal thickness. The area where passive margins extend
697 landward is determined by the limit of the continental crust before significant stretching occurs,
698 referred to as the unstretched continental crust limit (UCCL; Nemčok, 2016). Initially, a range of
699 crustal thickness can be estimated based on UCCL and subsequently refined during optimisation
700 along with other parameters. This optimisation process enables us to refine our understanding of
701 the crustal thickness evolution and its implications throughout the studied time span.
702 Specifically, we examined 12,870 combinations of the exponential stretching coefficient, rift
703 threshold length, strain rate resolution, and initial crustal thickness to find the optimal
704 configuration for our study. To evaluate the performance of each model, we utilised the
705 minimum Root Mean Square Error (RMSE) as our benchmark, comparing the calculated crustal
706 thickness at 0 Ma with the present-day GEMMA crustal thickness. This metric effectively
707 penalises outliers, providing a comprehensive assessment of model accuracy.
708



709
710
711
712
713

714 **Figure 7.** Results from our optimisation of 12870 combinations of the exponential stretching
715 coefficient, rift threshold length, strain rate resolution, and initial crustal thickness. We used
716 Root mean squared error (RMSE) calculated between crustal thickness estimates at 0 Ma and
717 known GEMMA crustal thickness model (Reguzzoni & Sampietro, 2015) as our performance
718 metric. Our optimisation results show that initial crustal thickness and exponential stretching
719 coefficient are the primary factor controlling model performance. a) RMSE for different values

720 of initial crustal thickness b) RMSE for different exponential stretching coefficient and edge
721 length threshold.

722

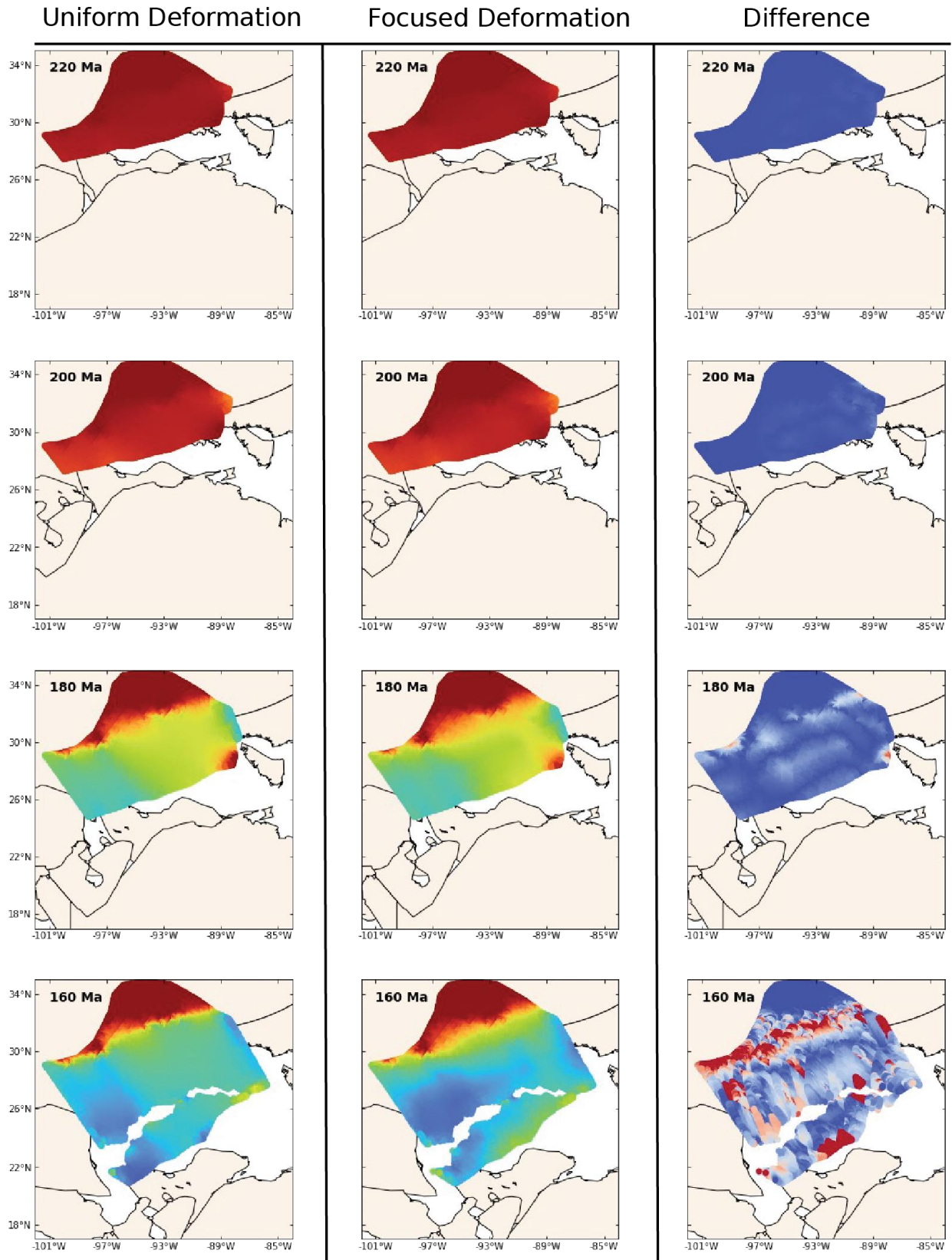
723 **4 Results**

724

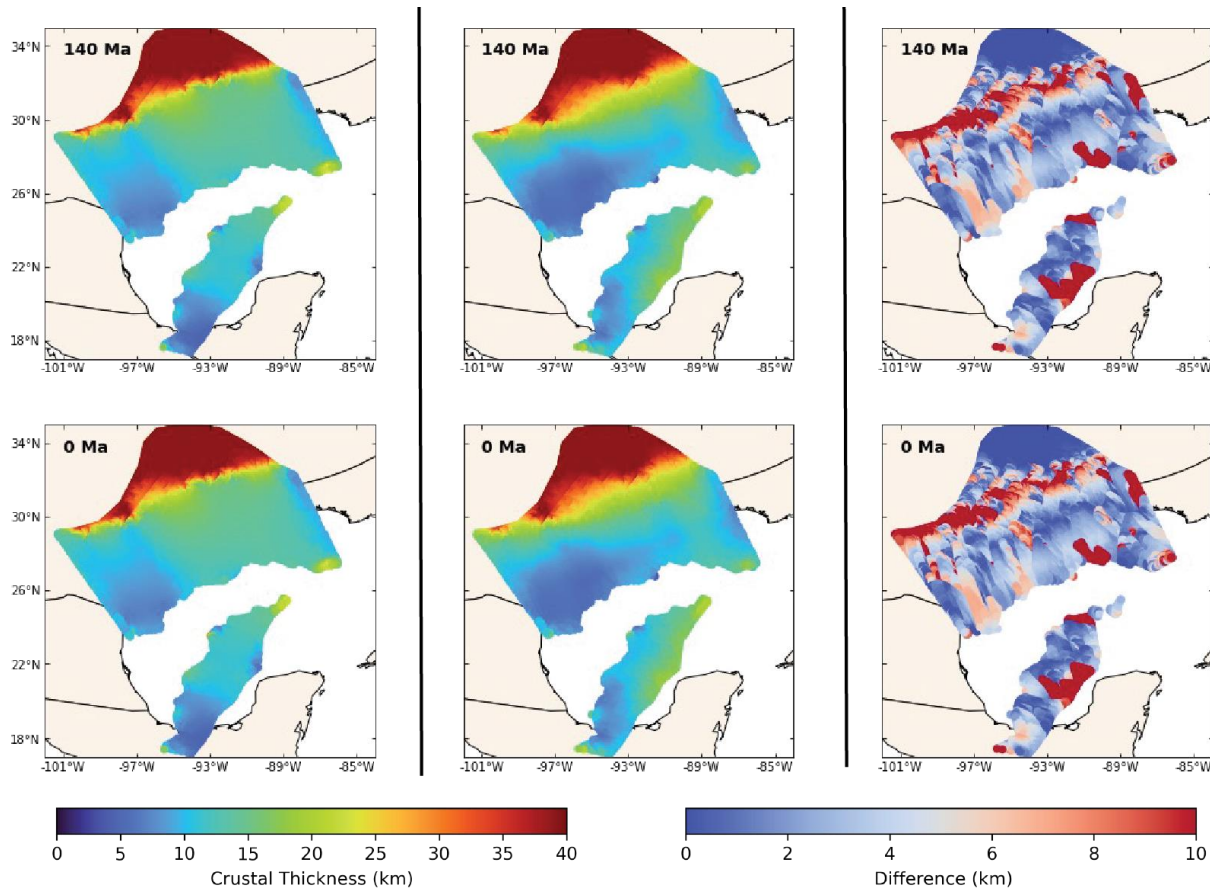
725 **4.1. Optimisation**

726

727 Analysis of the variation of RMSE with varying values of crustal thickness, exponential
728 stretching coefficient, and Edge Length Threshold revealed that the initial crustal thickness and
729 exponential stretching coefficient had the most significant impact on our model's performance
730 (Figure 7). Through testing, a global minimum model with an RMSE of 5.6 km was found that
731 had an exponential stretching coefficient of 5.3 and an estimated initial crustal thickness prior to
732 GoM stretching of 39 km. The crustal thickness estimates based on UCCL suggest a thickness of
733 38.4 ± 3.0 km for unstretched crust (Hosseinpour et al., 2013; Kaban et al., 2014; Reguzzoni &
734 Sampietro, 2015), which closely aligns with the optimized value obtained from the model.
735 Notably, the edge length threshold and strain rate resolution parameters, crucial for achieving the
736 closest match, fell consistently within the ranges of 2.25 to 2.75 and 10^{-16} to 10^{-17} , respectively.
737 When comparing our model with the uniform deformation model proposed by Müller et al.
738 (2019) for the same region, we found that our focused deformation model's RMSE outperformed
739 it by nearly 2.5 times in estimating crustal thickness. Additionally, our model exhibited excellent
740 agreement with the GEMMA crustal thickness model (Reguzzoni & Sampietro, 2015),
741 particularly in the eastern and western GoM regions, with an absolute error of ~ 1.5 km.



742
743
744



745
746

747 Figure 8: A comparison of crustal thickness between our uniform deformation model and
748 focused deformation model, where colored region demonstrates deformed continental crust.
749 During the early evolution from 230 Ma to 190 Ma, the crustal thickness shows similarities
750 spatially in both the uniform and focused deformation scenarios. However, from ~190 Ma to
751 ~175 Ma, a region of focused stretching emerges in the central GoM (see 180 Ma). Notably,
752 there is a significant disparity in crustal thickness estimation between the focused deformation
753 and uniform deformation models after the rifting event at ~160 Ma.

754

755

756 4.2 Evolution of stretching factor, crustal thickness, and tectonic subsidence

757

758 4.2.1 Early Triassic-Sinemurian (~230 Ma to ~190 Ma)

759

760 The initiation of continental rifting in the GoM traces back to the Triassic period when the
761 Yucatán block was coupled with the South America plate. During this stage, some extension
762 occurred between North America and Yucatán. According to our model, the region experienced
763 approximately 120 km of extension before the Yucatán block began drifting and undergoing
764 anticlockwise rotation. However, accurately determining the pre-rift position of the Yucatán
765 block poses challenges due to limited means of estimating internal extension caused by rifting
766 and the ongoing debate surrounding the definition of the Yucatán block itself. For instance,
767 recent research has suggested that the Chuacús Complex, once considered part of Yucatán, is

768 allochthonous due to its distinct high-pressure, low-temperature metamorphic characteristics
769 (Maldonado et al., 2018).

770

771 During the initial phase, the extension was relatively uniform along a north-south direction,
772 characterised by minimal stretching ($\beta = 1.1$) and crustal thinning (Figure 8). The gradual
773 stretching process resulted in the development of low strain rates ($6 \times 10^{-16} - 4.0 \times 10^{-16} \text{ s}^{-1}$)
774 evenly distributed across the region. However, tectonic subsidence calculations reveal lateral
775 variation in the east-west direction, leading to the creation of accommodation for the deposition
776 of Triassic sediments (Figure 9 and 10). The western GoM exhibited approximately 1.5 km of
777 tectonic subsidence, gradually decreasing towards the central GoM (Figure 10). Similarly, the
778 eastern GoM region adjacent to the SGR showcased a similar value (~ 1.2 km) of subsidence.

779

780 **4.2.2 Pliensbachian-Toarcian (~190 Ma to ~175 Ma)**

781

782 The opening of the Proto-Caribbean basin triggered the rotation of the Yucatán block, leading to
783 significant extension of GoM continental crust. During this phase, our model indicates a rapid
784 tectonic subsidence of 3–5 km between North America and Yucatán. However, the zone of
785 stretching exhibits spatial variability. As the Yucatán block drifted southward, the strain rate
786 within the deformation zone increased, from $4.0 \times 10^{-16} \text{ s}^{-1}$ to $1.7 \times 10^{-15} \text{ s}^{-1}$, resulting in more
787 focused deformation in the region between blocks. Our model allows for the adjustment of the
788 deformation mesh, concentrating the extension within the region of necking. Notably, our results
789 highlight the development of a focused stretching zone that propagated from the western to
790 eastern region of the GoM. In contrast, the uniform deformation model failed to capture this
791 focused region of thinning, particularly in the central and eastern GoM (see snapshots 180 Ma
792 and 160 Ma in Figure 8).

793

794 We find that rapid tectonic subsidence initiated in a wider zone in the western GoM and a
795 narrower zone in the central and eastern GoM during the Pliensbachian period (~ 185 Ma) and
796 then propagated to create a wider central and western GoM by the Bajocian period (~ 170 Ma).
797 Tectonic subsidence reached approximately 4–5 km in the western GoM and 2–3 km in the
798 eastern GoM, revealing lateral variations in the accommodation within the GoM prior to its
799 opening (Figure 10). However, our model indicates that this heightened subsidence was confined
800 to the region of focused stretching rather than being uniformly distributed across the basin. We
801 observe significant stretching, with the β value transitioning from 1.1 at the start of the Early
802 Jurassic to a value greater than 4 by the end of the Early Jurassic, resulting in substantial crustal
803 thinning (Figure 11). Additionally, the overall stretching occurred in a wider zone in the western
804 GoM compared to the central and eastern regions. Our crustal thickness calculation demonstrates
805 that during the Pliensbachian period, the western GoM experienced considerable thinning, with
806 an average thickness of 17 km, while the central and eastern regions of the GoM thinned to an
807 average thickness of 26 km (Figure 8).

808

809

810 **4.2.3 Middle-Late Jurassic (~175 Ma to ~145 Ma)**

811

812 During the Toarcian to Callovian periods, the western GoM experienced substantial thinning due
813 to the intensified extension caused by the anticlockwise rotation of the Yucatán block.

814 Consequently, the average crustal thickness in this region decreased to less than 10 km.
815 Furthermore, the western GoM exhibited higher tectonic subsidence compared to the eastern
816 region. Although extension in the western GoM ceased in the Callovian (~166 Ma), it persisted
817 into the Early Oxfordian (~162 Ma) in the eastern GoM, albeit at a reduced rate (Figures 11 and
818 12). Considering the dominance of salt deposition during the Bajocian age and the limited
819 influence of outer-margin extension on the base-salt layer near the oceanic crust margins, it is
820 plausible to consider that the divergence of the northern GoM and Yucatán salt depocenters, as
821 well as the initiation of seafloor spreading, occurred as early as the Bathonian epoch.

822
823 Our model indicates that the zone of focused stretching propagated from west to east prior to the
824 onset of seafloor spreading. However, with the onset of seafloor spreading, our deformation
825 model reveals a stage-wise opening process. It commenced in the Bathonian in the western GoM,
826 followed by spreading in the central GoM during the Callovian and eventually reaching the
827 eastern GoM by the Oxfordian. Notably, an intriguing observation from our model is that the
828 seafloor spreading occurred south of the region of focused stretching, suggesting a possible rift
829 jump. Additionally, the spreading center exhibited asymmetry in both the eastern and western
830 GoM with respect to the focused stretching zone. However, in the central GoM, the spreading
831 center was in close proximity to the region of focused stretching. By the Kimmeridgian period
832 (~153 Ma), rotational seafloor spreading continued, accompanied by a similar but opposite
833 rotational seafloor spreading in the Proto-Caribbean Seaway. The second phase of drifting
834 commenced in the Tithonian, characterised by a gradually decreasing spreading rate.

835 836 **4.2.4 Cretaceous**

837
838 By the end of the Berriasian (~140 Ma), seafloor spreading in the GoM had significantly
839 decelerated. In the early Valanginian stage, the Yucatán block had reached its current position
840 relative to North America, indicating the possible completion of rotational seafloor spreading in
841 the GoM. The subsequent separation between the North and South American plates took place
842 exclusively within the Proto-Caribbean Seaway after this period. During this time, the GoM
843 experienced crustal cooling and entered a phase dominated by thermal subsidence, creating
844 ample space for the deposition of thick sedimentary layers. Following the extensional phase,
845 gradual conductive cooling of the lithosphere occurred, leading to increased density in both the
846 crust and mantle. In order to maintain isostatic equilibrium, the basin underwent gradual
847 subsidence. Throughout much of the Cretaceous period, the GoM was characterised by passive
848 tectonic conditions in most areas, with occasional localised interruptions caused by factors such
849 as igneous activity and thermal uplift in the eastern Texas region surrounding the Sabine Uplift.
850 Although these factors significantly influenced the tectonic subsidence of the basin, they could
851 not be accounted for in our model.

852 853 **5 Discussion**

854 855 **5.1. Initial rifting and red bed deposition**

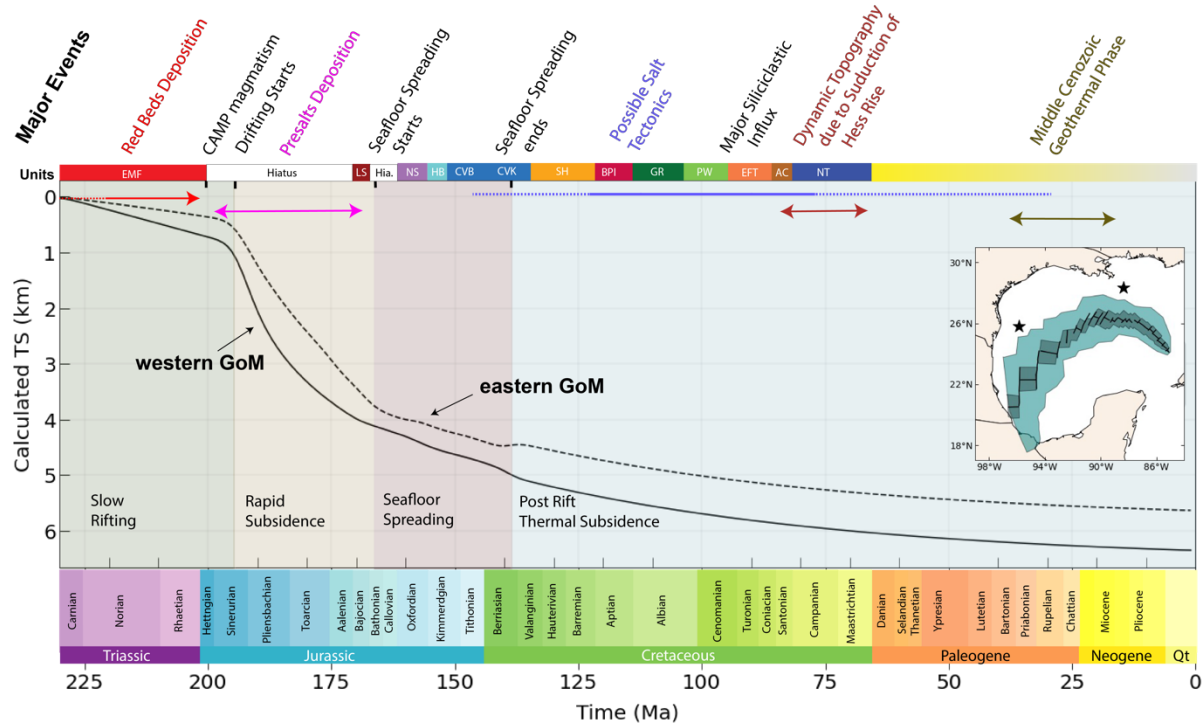
856
857 During the initial rifting phase prior to the anticlockwise rotation of the Yucatán block, our
858 model indicates ~1.5 km of subsidence, which would have created accommodation for the
859 deposition of red bed sediments. However, our tectonic subsidence calculation suggests that the

860 estimated thickness of red bed sediments from our model in the northern GoM is slightly lower
861 than the inferred thickness (Milliken, 1988). This observation may imply that the deposition of
862 red beds filled pre-existing accommodation spaces rather than depositing directly within a
863 graben. It is important to note that our tectonic subsidence calculation relies on the stretching
864 imposed by Yucatán motion, and we have limited constraints on the internal deformation of the
865 Yucatán block and the position of the mid-rift high. Moreover, our model may not be able to
866 capture high frequency, high amplitude changes in stratal thicknesses caused by brittle
867 deformation which can also be responsible for thicker red beds in northern GoM. Nonetheless,
868 our model offers valuable insights into how sediments might have been routed southward from
869 the Ouachita-Marathon region.

870
871 The initial tectonic subsidence of ~1.5 km in the eastern and western parts of the GoM, between
872 230 Ma and 190 Ma before the drifting stage suggests that sediment deposition routes were
873 bifurcated to the east and west within the narrow extensional zone between Yucatán and North
874 America. This is further supported by the presence of interior drainage systems extending across
875 various North American basement source terranes, as evidenced by diverse U-Pb age spectra
876 from pre-salt wells (Frederick et al., 2020; Snedden & Galloway, 2019). Detrital zircon data
877 from 16 wells show the existence of three distinct paleo drainage systems in the northern GoM
878 (Frederick et al., 2020), which aligns well with our model (Figure 10). The western paleo
879 drainage system extended from the highlands of Central Texas to the submarine Potosi Fan on
880 the western margin of Laurentia. Detrital zircon ages from the Eagle Mills sediments in this
881 region suggest tributary sources from the East Mexico arc, Yucatán/Maya, and Marathon-
882 Ouachita provinces, encompassing a range of detrital zircon ages (Frederick et al., 2020). The
883 southwestern flow was characterised by peri-Gondwanan detrital zircon ages from late Paleozoic
884 accreted basement and/or successor basins, while the southeastern fluvial networks originated
885 from traditional North American basement provinces, including Grenville, Mid-Continent, and
886 Yavapai-Mazatzal. The southern paleo drainage system in the north-central GoM region is
887 bifurcated around the Sabine and Monroe uplifted terranes (Figure 10). The eastern paleo
888 drainage system exhibited a regional southward flow, with pre-salt detrital zircon ages
889 predominantly indicating local Gondwanan/peri-Gondwanan sources, such as the proximal
890 Suwannee terrane and Osceola Granite complex (Frederick et al., 2020).

891
892 Our model suggests that these paleo drainage systems likely served as the sources of basin fill in
893 the GoM (Figure 10). The creation of accommodation in the western GoM facilitated the
894 deposition of red bed sediments through the western paleo drainage system and the western
895 branch of the bifurcated southern paleo drainage routes. Similarly, tectonic subsidence in the
896 eastern GoM region would have also provided space for sedimentation in the eastern branch of
897 the southern paleo drainage system and the eastern paleo drainage system.

898



899
 900 **Figure 9.** Tectonic subsidence calculation from our model. Four stages can be used to describe
 901 the tectonic evolution of the GoM basin. Slow rifting Phase: In this phase, there is small tectonic
 902 subsidence creating accommodation for infilling the GoM basin with red beds. Rapid
 903 Subsidence: Following the rift-drift transition, there is rapid subsidence which resulted in 3-4 km
 904 of subsidence. This led to the deposition of pre-salts. Seafloor Spreading Phase: The Louann
 905 salts have already been deposited. First, the western GoM opened, followed by the eastern GoM.
 906 Post-Rift Thermal Subsidence: The last stage is marked by conductive cooling of the lithosphere
 907 resulting in gradual tectonic subsidence. The difference in tectonic subsidence in western GoM
 908 and eastern GoM further increases. Most of the later secondary tectonic activity (Major events in
 909 color) would have influenced the tectonic subsidence and has not been accounted for in this
 910 study. Abbreviations: EMF, Eagle Mills Formation; LS, Louann Salt; NS, Norphlet-Smackover
 911 Formations; HB, Haynesville-Buckner Formations; CVB, Cotton Valley-Bossier; CVK, Cotton
 912 Valley-Knowles; SH, Sligo-Hosston; BPI, Bexar-Pine Island; GR, Glen Rose; PW, Paluxy-
 913 Washita; EFT, Eagle Ford-Tuscaloosa; AC, Austin Chalk; and NT, Navarro-Taylor.

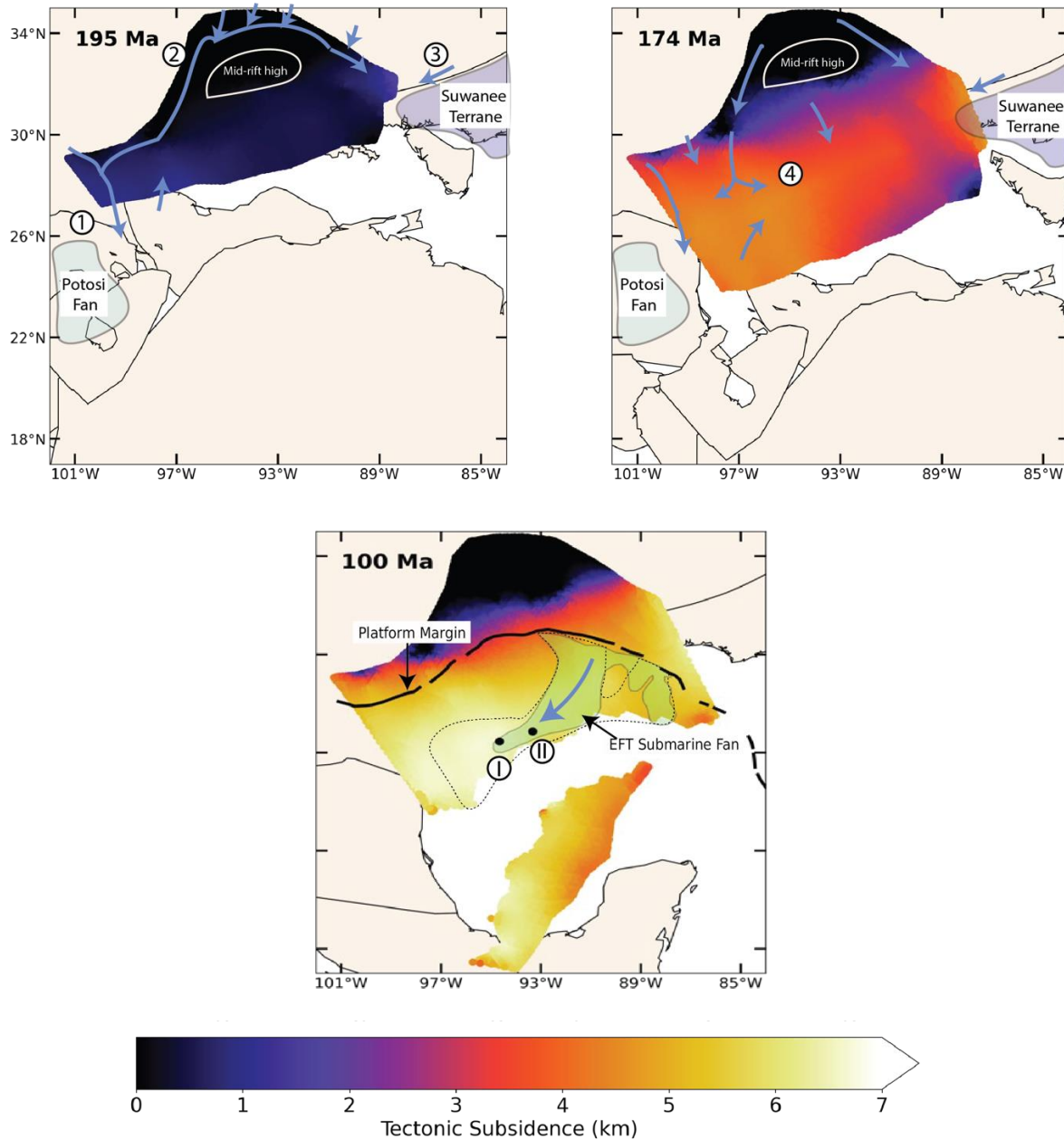
914 915 **5.2 Rapid subsidence and pre-salt deposition**

916
 917 The ~40 Myr hiatus between the syn-rift red bed deposits and the Louann salt deposits in the
 918 Eagle Mills Formation poses an important conundrum. Zircon analysis from the Wood River
 919 Formation of the South Florida Basin and outcrops of the Dockum Group north of the Ouachita-
 920 Marathon orogenic belt indicates deposition ages of approximately 235–195 Ma (Wiley, 2017)
 921 and 234–200 Ma (Umbarger, 2018), respectively, leaving a gap between the Louann Salt and the
 922 Triassic deposits (Dickinson et al., 2010). Limited exposure of early Mesozoic outcrops south of
 923 the Ouachita Mountains and only few drilled wells below the autochthonous Louann Salt in the
 924 onshore USA, makes the geological record in the western GoM after the Permian period unclear
 925 (Snedden & Galloway, 2019). For example, there is a 90 Myr gap between the Permian strata

926 and the earliest fully marine Upper Smackover strata formed during the middle Mesozoic drift
927 and cooling phase of the GoM basin in west Texas (Snedden & Galloway, 2019). Seismic
928 surveys conducted along the Yucatán margin and the eastern GoM reveal interpretations of
929 several km thick pre-salt sediments (see section 2.3). Understanding the formation of pre-salt
930 deposits in this area is crucial because, if these deposits are red beds, they can serve as source
931 rocks for stratiform copper deposits that typically form during the early stages of rifting through
932 basin-wide fluid flow systems (Gustafson & Williams, 1981; Hitzman et al., 2005). Evaporites
933 overlying red beds often provide a source of sulphide that is also important for forming
934 sediment-hosted stratiform copper deposits (Sawkins, 1990). Pre-salt strata in the GoM are
935 covered by a thick layer of Louann Salt, and the presence of red beds as copper source rocks may
936 indicate that with optimal thermal and hydrological conditions present may indicate potential for
937 sediment-hosted stratiform copper deposits. Our tectonic subsidence model provides valuable
938 insights necessary to characterize the deposition of these pre-salt strata.

939
940 Our model suggests that the onset of Yucatán rotation triggered a sudden increase in tectonic
941 subsidence (Figure 9), creating ample accommodation for sedimentation prior to the marine
942 incursion. The region of high tectonic subsidence shifted further south near the Yucatán margin,
943 implying approximately 4-5 km of tectonic subsidence in the focused stretching zone, and
944 suggesting the presence of a thick pre-salt sedimentary layer. This aligns with the current
945 understanding of a pre-salt sedimentary basin, as mapped by seismic and potential field data
946 (Filina, 2019), indicating continuous deposition. Our model suggests a wider region for pre-salt
947 deposition in the western GoM compared to the eastern parts, with higher tectonic subsidence
948 values near the Yucatán margin, indicating thicker sediment in that area. We propose that the
949 sudden increase in accommodation in the southern GoM, close to Yucatán, facilitated the
950 deposition of sediments from the northern central GoM into the present-day pre-salt sedimentary
951 basin. While the rifting and red bed deposition was continuous until salt deposition, the zone of
952 deformation shifted southward, near the Yucatán margin, which is currently covered by the salt
953 canopy and lacks comprehensive penetrations. As a result, the western paleo drainage and the
954 western branch of the southern paleo drainage actively filled the newly created accommodation
955 by passing previous basin (Figure 10), potentially explaining the larger hiatus between the red
956 beds and the beginning of the Louann Salt in the northern GoM.

957



958

959 **Figure 10.** A successor basin fill model showing that a large area in the central GoM may have been filled with red bed sedimentation. Sediment routing was based on an analysis of key wells and their detrital zircon geochronology, which reveals the direction of sediment routing trends (Snedden & Galloway, 2019). 1) The western paleo drainage systems 2) The southern paleo drainage systems have bifurcated around midrift high into two branches: eastern and western branches. 3) The eastern paleo drainage systems. Our model shows tectonic subsidence along these paleo drainages (Right). Our model shows development in rapid tectonic subsidence in a focused region (4). Proposed model and sediment routing for pre-salts deposition based on our tectonic subsidence calculation (left).

960
961
962
963
964
965
966
967

968 This region is wider in the western part of GoM; however, it gets narrower as we move toward
969 the east. We propose that the sedimentation was a continuous process in GoM. However, due to
970 the creation of accommodation during rapid subsidence, the red bed deposition shifted further
971 south near the Yucatán margin. Moreover, western paleo drainage, as well as the western branch
972 of southern paleo drainage, would have been a major source of these sediments. Cenomanian-
973 Turonian (Ceno-Turonian) EFT submarine fans, originating from the southern Louisiana
974 platform margin and extending towards the Tiber (II) and BAHA II (I) well locations in the
975 western GoM (Snedden et al., 2016). Well data is limited further west in the deepwater of the
976 GoM. However, our model suggests that these submarine fans may have extended even farther
977 west, beyond the range of current well penetration, due to increasing differential subsidence
978 towards the west.

979

980 **5.3 Evolution of Rifting**

981

982 The accurate determination of the crustal nature in the GoM has been challenging due to the lack
983 of wells penetrating basement. However, recent seismic reflection data from the northern and
984 western Yucatán and northern GoM reveal evidence of magmatism (see section 2.4; Figure 2).
985 The presence of high-amplitude magnetic anomalies coinciding with the SDRs further supports
986 this history of magmatism. Additional geophysical observations, such as the presence of high-
987 velocity crustal intrusions in the lower crust, lend further support to the magma-rich hypothesis
988 (Filina et al., 2022; Steier & Mann, 2019). Velocity models derived from refraction data over
989 distinct high FMAs indicate a high-velocity lower crust in the same region as the interpreted
990 SDRs (Eddy et al., 2014). The inboard Apalachicola Basin (Figure 1) harbors a significant syn-
991 rift volcanic fill (Minguez et al., 2020). Although intriguingly, these features are not positioned
992 at the transition to the oceanic crust (Figure 2). Another common observation in magma-rich
993 margins is the presence of SDRs and lower crustal intrusions, resulting in an abnormally thick
994 crust, presumably formed through subaerial accretion, transitioning into classic submarine
995 oceanic crust which are ~ 7 km thick (Funck et al., 2017; Kelemen & Holbrook, 1995).

996 However, the GUMBO4 line exhibits a relatively thin (~5 km) and uniform oceanic crust, which
997 indirectly supports a magma-poor interpretation (Eddy et al., 2014). The presence of ridge-like
998 basement highs in seismic reflection (Pindell et al., 2014) further supports the magma-poor
999 hypothesis. The examination of aeromagnetic data also reveals compelling indications pointing
1000 towards the presence of serpentinised mantle that has been exhumed along the northern margin
1001 of the GoM (Minguez et al., 2020; Pindell et al., 2016). Additionally, recent seismic reflection
1002 profiles serve as further evidence, illustrating the existence of distinct segments featuring
1003 exhumed mantle, alongside occurrences of magmatic intrusion or extrusion along the margins of
1004 the Yucatán region (Izquierdo-Llavall et al., 2022). Consequently, an ongoing debate persists
1005 regarding whether the GoM can be classified as magma-rich or magma-poor.

1006 The extent of magmatism during the rifting stage is influenced by several factors, including
1007 mantle temperature, extension rates, mantle composition, preceding rift history, and the presence
1008 or absence of hot active upwelling of the asthenosphere (Armitage et al., 2010; Tetreault &
1009 Buitter, 2018; Tugend et al., 2020; White & McKenzie, 1989). Among these factors, mantle
1010 temperature is considered the most crucial, as it governs the onset of decompression melting
1011 (Tugend et al., 2020). Elevated mantle temperatures increase magma supply, resulting in higher
1012 volumes of magmatism in magma-rich margins (White & McKenzie, 1989). The rate of
1013 lithospheric extension during breakup is another critical factor that significantly influences

1014 magma supply (Armitage et al., 2010). Magma-rich margins tend to form under conditions where
1015 plate separation occurs at a faster pace than in magma-poor margins (Lundin et al., 2014).
1016 Mantle composition also plays a role in the volume of melt production with more primitive and
1017 volatile-rich mantles generating greater amounts of melt (Cannat et al., 2008). Therefore, the
1018 level of magmatism observed at the rift margin and within the GoM is dependent on the complex
1019 interaction of these parameters. Our reconstructions provide valuable insights into the temporal
1020 and lateral variations in magmatism throughout the evolution of the GoM. Based on the
1021 stretching factor, crustal thickness, and extension rate evolution derived from our model, we
1022 propose a two-phase development of the GoM's crustal architecture.

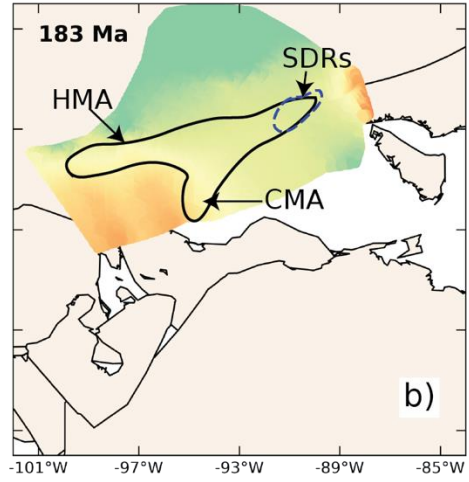
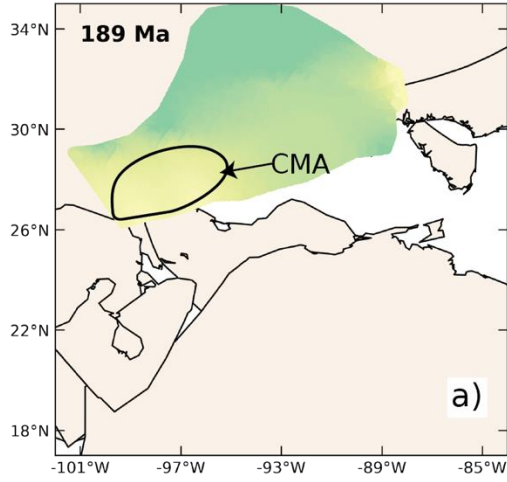
1023

1024

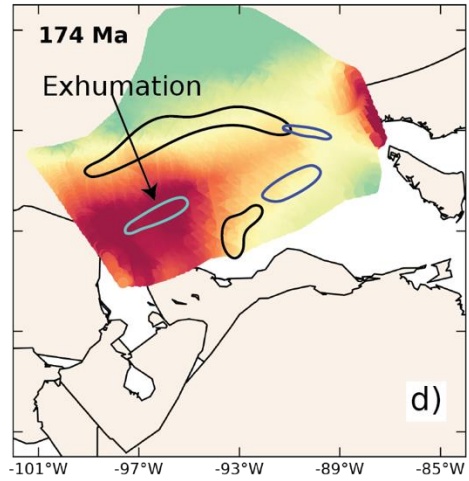
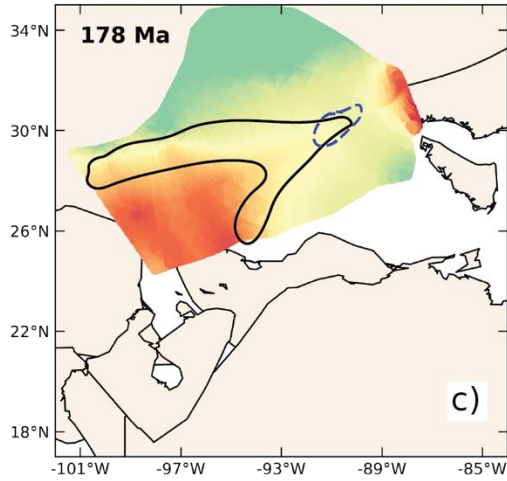
1025

1026

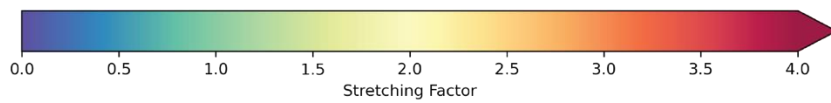
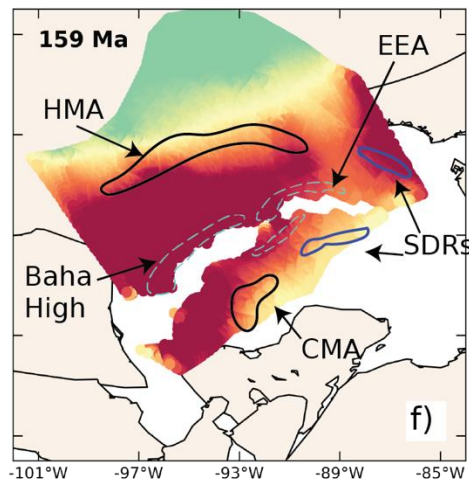
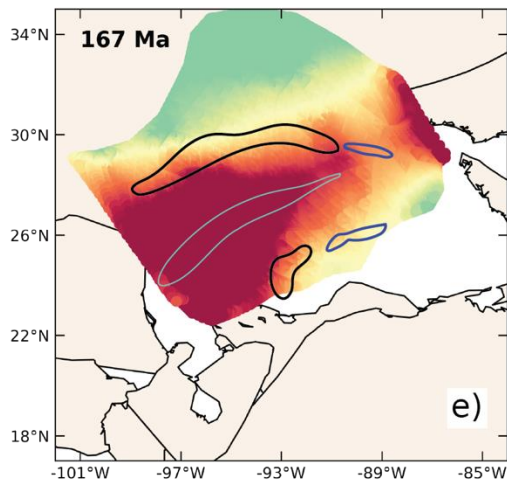
Magma Rich Phase



Hyperextension



Exhumation



1028 **Figure 11.** a) Formation of CMA aligns well with crustal thinning suggesting rift-related
 1029 volcanism b) Formation of HMA, LMA, and SDRs. c) Hyperextension started in western GoM.
 1030 d) Hyperextension propagated to eastern GoM and separation of CMA and HMA. Note HMA,
 1031 CMA, and SDR have undergone deformation owing to the motion of Florida and Yucatán block
 1032 motion. Exhumation might have started in western GoM, leading to the formation of BAHA
 1033 high. e) Seafloor spreading starts. Exhumation in eastern GoM resulting in EEA. f) SDR
 1034 undergoing deformation owing to the motion of Florida Block. Symmetric and Conjugate EEA
 1035 separated in central GoM. However, further west, the EEA is asymmetric and tapers out.
 1036 Magnetic anomalies and SDRs are in black and blue, respectively. The solid light blue color
 1037 polygon represents the location of possible exhumation. Dashed light blue polygons represented
 1038 reconstructed BAHA high and EEA anomalies, respectively. Polygons in beige color are rigid
 1039 continent block.

1040

1041 5.3.1 Magmatism

1042

1043 The transition from rifting to seafloor spreading in passive rift margins occurs when the
 1044 stretching factor exceeds a certain threshold (Le Pichon & Sibuet, 1981). Volcanic activity is
 1045 more likely to occur in passive rift margins when the stretching factor exceeds approximately 2
 1046 (Le Pichon & Sibuet, 1981). Our model reveals a link between crustal thinning and the
 1047 formation of the HMA, CMA, and LMA in the western GoM, as well as the positioning of SDRs
 1048 in the eastern GoM. The CMA in the western GoM formed near the Yucatán margin during the
 1049 Sinemurian period. As deformation progressed, the region stretched, leading to the formation of
 1050 the HMA (Figure 11b). Deep seismic data suggest that the FMA and CMA are likely associated
 1051 with volcanic flows within the syn-rift sections of rift basins (Mickus et al., 2009). The
 1052 occurrence of the HMA in the western GoM during the Sinemurian period may also be linked to
 1053 magmatic activity, similar to the CMA. In the eastern GoM, the SDRs observed off the Yucatán
 1054 margin coincide with the YMA (Steier and Mann, 2019; Filina and Hartford, 2021; Filina and
 1055 Beutel, 2021). The refraction velocity model (Eddy et al., 2014) indicates that the same region
 1056 where the SDRs were interpreted in the FMA exhibits a high-velocity lower crust and a Moho
 1057 associated with intrusions. Liu et al. (2019) have modelled SDRs reflections with high magnetic
 1058 susceptibilities and densities, which fit well with the potential field data.

1059 One possible explanation for the formation of these SDRs and magnetic anomalies is their
 1060 proximity to the CAMP event in eastern North America. The elevated subcontinental mantle
 1061 temperature during the CAMP event would have led to increased decompressional melt
 1062 generation, resulting in magmatism and lower crustal intrusions (Figure 12). However, the extent
 1063 of this magmatism would have been limited due to the relatively short duration of the CAMP
 1064 event. A similar process has been proposed to explain rifting in the northwest Indian Ocean,
 1065 where the presence of the Deccan Traps, located 1000 km away from the rift zone, created a
 1066 thermal anomaly that triggered igneous intrusion along the Gopi Rift (Armitage et al., 2010).
 1067 However, this thermal anomaly was eventually depleted, leading to the formation of a magma-
 1068 poor Laxmi Ridge margin (Armitage et al., 2010). The production and emplacement of magma
 1069 during the formation of the GoM might have varied laterally, which could explain the presence
 1070 of SDRs along the eastern GoM due to its proximity to the CAMP event. Alternatively, the HMA
 1071 may also be related to the SDRs, but due to its depth and thick salt cover, it remains challenging
 1072 to determine the presence of SDR patterns in the seismic sections. Another plausible reason for
 1073 the reduced occurrence of magmatic SDRs in the western GoM could be hindered melt

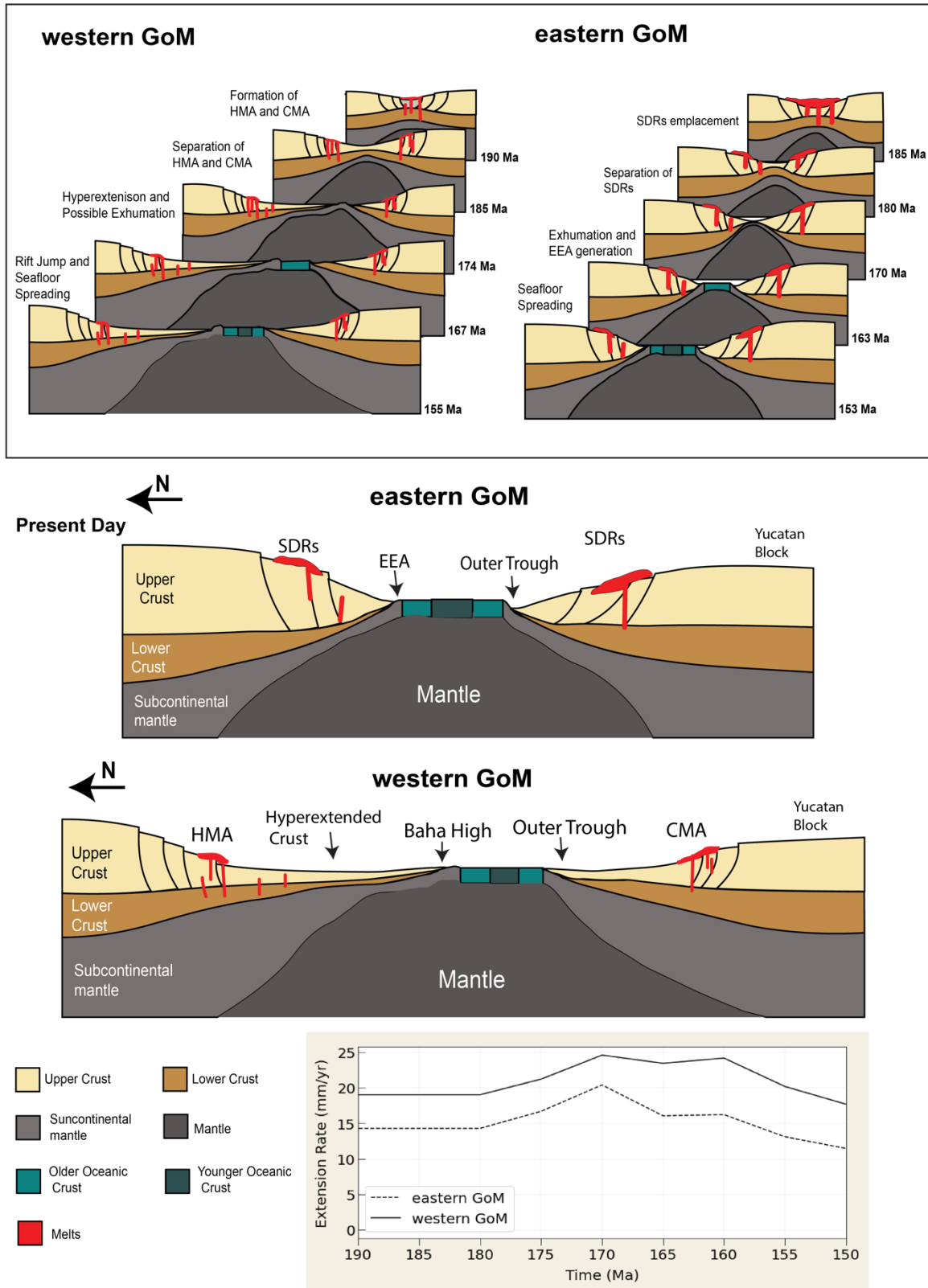
1074 extraction caused by the greater lithospheric thickness in that region (Izquierdo-Llavall et al.,
1075 2022). Furthermore, our model indicates that due to the motion of the Florida Bahamas and
1076 Yucatán blocks, these SDRs would have experienced significant deformation and later became
1077 separated from each other as a result of seafloor spreading, resulting in their present-day
1078 locations (Figure 11 and 12).

1079

1080

1081

1082



1083
1084
1085
1086

Figure 12. Summary of the evolution of the GoM crustal architecture. Our model suggests that the Mesozoic evolution of the eastern and western GoM basins (roughly along profile GUMBO1

1087 and GUMBO3: Figure 3) commenced as a magma-rich margin. During the Pliensbachian period,
1088 there were occurrences of magmatic intrusions and extrusions, resulting in the formation of the
1089 HMA, CMA, and LMA in the western GoM, as well as the SDRs in the eastern GoM. The
1090 elevated subcontinental mantle temperature during the CAMP event likely caused increased
1091 decompressional melt generation, leading to magmatism and lower crustal intrusions. However,
1092 this magmatism was short-lived. The subsequent Toarcian development indicates a magma-poor
1093 origin characterized by hyperextension and potential mantle exhumation. The rate of extension
1094 plays a significant role in shaping the crustal architecture. Higher extension rates (>20 mm/yr)
1095 facilitate rapid upwelling of the mantle, resulting in exhumation. As the extension rate is higher
1096 farther from the pole of rotation, the western GoM underwent more thinning and wider
1097 hyperextension.

1098

1099 **5.3.2 Hyperextension and Exhumation**

1100

1101 The phase of magma-rich rifting in the GoM was relatively brief due to the short-lived CAMP
1102 event. Following the transition from rift to drift, our results indicate a wider region of thinned
1103 crust in the western GoM, indicating hyperextension (Figure 11). However, this region narrows
1104 as we move towards the central and eastern GoM. In the Bay of Biscay, Le Pichon and Sibuet
1105 (1981) estimated that a $\beta > 3.2$ was required for the formation of oceanic crust, and for magma-
1106 rich margins, these values are even lower. However, our calculations suggest that if this were the
1107 case in the GoM, the formation of oceanic crust would have commenced sooner, and further
1108 north than currently predicted based on stretching factors. Our analysis reveals a β value of 4 in
1109 the wider western GoM basin during the early Toarcian period, while the eastern GoM exhibits a
1110 β value of 1.5, and that too within a narrow zone. However, by the late Aalenian-early Bajocian
1111 period, the eastern GoM shows a β value of approximately 4, whereas the western GoM reaches
1112 around 5.2. This suggests that the rift propagation occurred from west to east, gradually
1113 ‘unzipping’ this hyperextended crust (Figure 11). The unzipping process was triggered by the
1114 anticlockwise rotation of the Yucatán block around the rotation pole located in the Florida
1115 Straits.

1116

1117 Notably, the extension rate plays a significant role in shaping the crustal architecture of an
1118 extending continental crust and its distance from the rotation pole affects the extension rate
1119 (Lundin et al., 2014). Closer to the rotation pole, the linear rate of plate extension is relatively
1120 small, resulting in a proximal margin characterised by limited extension, where the brittle-ductile
1121 transition remains in the crust and brittle deformation occurs along high-angle faults (Colletta et
1122 al., 1988). As we move farther away, deformation progresses into the thinning phase, where the
1123 complete embrittlement of the crust, fault penetration, and mantle serpentinitisation become likely
1124 (Lundin et al., 2014). At an even greater distance from the pole, mantle exhumation is predicted.
1125 Eventually, the pole of rotation becomes so distant that the linear half-spreading rate exceeds the
1126 critical velocity for melting (Bonatti, 1985; Chu & Gordon, 1998). In the case of the GoM, a
1127 similar explanation can be applied to understand the crustal architecture. The interpretation of
1128 GUMBO1 by van Avendonk et al. (2015) reveals the thinning and wider hyperextension of the
1129 continental crust with an exposed upper mantle in the western GoM, which is situated farther
1130 away from the rotation pole (Figure 4). Additionally, analogue rock properties-based modelling
1131 of the EEA suggests the presence of a narrower zone of exhumed serpentinitised mantle along the
1132 eastern GoM (Minguez et al., 2020). Recent seismic reflection profiles also indicate segments of

1133 exhumed mantle (Izquierdo-Llavall et al., 2022). These observations, along with the extension
1134 rate derived from our model, suggest that by the end of the Early Jurassic, the western GoM
1135 would have experienced a prolonged period of hyperextension followed by mantle exhumation
1136 prior to seafloor spreading (Figure 12). Moreover, numerical models have demonstrated that
1137 extension rates exceeding 20 mm/yr facilitate rapid upwelling of the mantle, leading to an
1138 increase in lower crust temperature, ductile deformation, and a decrease in viscosity (Tetreault &
1139 Buiter, 2018). Such high extension rates cause the strain in the mantle to decouple from the crust,
1140 creating a pathway for exhumation and generating a counterflow in the mantle.
1141 Although our model cannot account for the uplift due to the mantle exhumation process,
1142 extension rate calculations from our model can be useful in understanding the evolution of
1143 hyperextension phase. Our extension rate calculations suggest that the western GoM experienced
1144 a high extension rate (>20 mm/yr) around the middle Toarcian period (~ 177 Ma). However,
1145 during the same period, the eastern GoM exhibited a lower extension rate (Figure 12).
1146 Nevertheless, by the late Aalenian period (~ 171 Ma), the eastern GoM underwent a high
1147 extension rate conducive to exhumation, resulting in the formation of symmetric and conjugate
1148 EEA. In the western GoM, the magnetic anomaly pattern and seismic results are less clear, but
1149 the presence of BAH high suggests hyperextension and possible mantle exhumation around the
1150 middle to late Toarcian. Furthermore, with a shift in extension rate from high to moderate, a rift
1151 jump likely occurred, with a more pronounced effect in the wider western GoM compared to the
1152 narrower eastern GoM. For a rift jump to occur, Tetreault & Buiter (2018) proposed that a region
1153 must be wide enough for the mantle upwelling to reach a depth where it interacts with the ductile
1154 lower crust. The deflection of strain by the ductile crustal layers towards the edge of the rift can
1155 then shift the upwelling to the rift's edge, abandoning the original rift (Brune et al., 2017;
1156 Naliboff & Buiter, 2015). This scenario may have occurred in the western GoM due to its wider
1157 zone of extension, resulting in a rift jump and the final margin structure characterised by one
1158 narrow margin (Yucatán) and the other with a wider, more hyperextended crust (north-western
1159 GoM). As seafloor spreading initiated in the western GoM, the eastern GoM experienced
1160 extension within a narrower zone, which likely prevented complete decoupling of the lower
1161 crust, resulting in a more symmetrical exhumation pattern.

1162

1163 **5.3.3 Post-Rift Thermal Subsidence**

1164

1165 The early Cretaceous period was characterised by seafloor spreading, followed by a gradual
1166 cooling of lithosphere that resulted in slower thermal subsidence following the stretching and
1167 thinning of the lithosphere (Figure 9). Prior to seafloor spreading, the earliest basin-wide
1168 deposits in the GoM basin were the Louann salt (Pindell et al., 2021). Following that, the
1169 Oxfordian Norphlet-Smackover Formations (NS) were deposited over the salts, resulting in salt-
1170 detached raft blocks in a region outlined by the Florida Escarpment, centred on western DeSoto
1171 Canyon and eastern Mississippi Canyon (Snedden & Galloway, 2019). Reconstruction of these
1172 blocks indicates a south-west direction of rafting by gravity gliding with NS as pre-kinematic
1173 and Haynesville-Buckner (HVB), Cotton Valley-Bossier (CVB), and Cotton Valley-Knowles
1174 (CVK) synkinetic units deposited at the same time as seafloor spreading (Pilcher et al., 2014;
1175 Snedden & Galloway, 2019). Our model suggests that the increase tectonic subsidence towards
1176 the rift zone, as well as from the east to west (Figure 9) can explain the formation of a
1177 seaward paleo-slope allowing gravity gliding of raft blocks in the south-west direction.

1178 Our tectonic subsidence suggests a slow increase in tectonic subsidence in the Middle Cretaceous.
1179 However, most this period was dominated by carbonates, resulting in the formation of an
1180 extensive platform-margin reef system in the northern GoM, which served as an effective barrier
1181 preventing siliciclastic sediment from reaching the deep GoM basin, where there was high
1182 tectonic subsidence (Snedden & Galloway, 2019). During the Cenomanian-Turonian period,
1183 local tectonics and drainage pattern expansion allowed siliciclastic sediment to reach deeper
1184 parts of the basin (Snedden & Galloway, 2019). This is evident from the presence of the Eagle
1185 Ford-Tuscaloosa (EFT) sandstones which span from the southern Louisiana platform margin to
1186 the deepwater of Keathley Canyon and Alaminos Canyon (Snedden et al., 2016). These fluvial-
1187 deltaic deposition systems have been discovered in a number of wells as far west as the Baha II
1188 well and the Tiber well (Figure 10). Mapping of these depositions through deep water well of
1189 GoM suggests a possible westward deflection (Snedden et al., 2016). Our model suggests that
1190 this westward deflection might be influenced by the differential tectonic subsidence in east to
1191 west direction. This indicates that the initial tectonic subsidence generated by rifting can have
1192 long-term consequences for depositional systems, altering their orientation long after rifting has
1193 ceased. Although there is limited deep well in western GoM but our model suggests EFT
1194 submarine fan extends further in western GoM (Figure 10).

1195
1196 Sediments from nearby region accumulated in the GoM over millions of years, significantly
1197 deepening the basin (Snedden & Galloway, 2019). The presence of vast Louann deposits and
1198 accompanying anhydrites, which were covered by sedimentary rocks, contributed to salt
1199 tectonics, making precise estimation of the tectonic subsidence value difficult (Ventress et al.,
1200 1989). The later Cretaceous subduction of Hess Rise into western North America also influenced
1201 tectonic subsidence by an estimated 2-3 km (Wang et al., 2017). These elements, while
1202 significant, have been eliminated from our estimation of tectonic subsidence.

1203
1204 Our model provides a comprehensive understanding of the GoM's evolution, encompassing the
1205 rift development and the evolution of GoM crust architecture. Furthermore, it offers insights into
1206 tectonic subsidence during the early phase of GoM opening, shedding light on the creation of
1207 accommodation for the deposition of red beds and pre-salt sediments before seafloor spreading.
1208 Overall, our model presents a novel approach to simulating the evolution of a passive rift margin
1209 using deformable plates. In older passive margin basins where optimization with present-day
1210 crustal thickness is not feasible, our model's parameters, such as the edge length threshold and
1211 strain rate resolution, can be employed. However, the initial crustal thickness and exponential
1212 stretching coefficient should be chosen thoughtfully, considering the extent and duration of
1213 extension. In scenarios where estimating tectonic subsidence from back-stripped data is
1214 challenging due to limited sedimentation during the early phase of rifting, our optimised model,
1215 constrained by known back-stripped tectonic subsidence or other geophysical data, becomes a
1216 valuable tool.

1217 1218 **6 Conclusion**

1219
1220 Our research introduces an optimised focused deformable plate reconstruction model for highly
1221 accurate reconstruction of the GoM's Mesozoic history. Our results reveal that initial tectonic
1222 subsidence occurred in the eastern and western regions of northern GoM during the Late
1223 Triassic, indicating the infilling of successor basin along three distinct paleo drainage systems.

1224 Furthermore, our reconstruction model demonstrates that the rapid increase in tectonic
1225 subsidence near Yucatán in the southern GoM led to sediment deposition in the present-day
1226 basin largely bypassing the previous successor basin. The hiatus between the Triassic Red beds
1227 and Bajocian salts in northern GoM can thus be attributed to this southward shift in the
1228 depocenter.
1229 Our model supports a hybrid origin for the GoM, characterised by an initial phase of magma-rich
1230 margins that transitioned into magma-poor margins, exhibiting temporal variability in
1231 magmatism. Magmatism in the GoM occurred during the Sinemurian period, resulting in the
1232 formation of SDRs. The HMA, LMA, and CMA coincided with crustal thinning in the western
1233 GoM, suggesting a magma-rich origin for this margin. However, our model also indicates
1234 prolonged hyperextension prior to seafloor spreading during the Pliensbachian-Toarcian.
1235 Through focused deformation, we demonstrate the propagation of rift through the unzipping of
1236 hyperextended crust from west to east, explaining the distinct crustal architecture observed in the
1237 GoM basin. The stretching factor and extension rate calculations derived from our model suggest
1238 that the western GoM exhibits a wider hyperextended crust with potential mantle exhumation,
1239 which likely occurred during the middle Toarcian. In contrast, the eastern GoM displays a
1240 narrower and more symmetric mantle exhumation during the Late Aalenian-Early Bajocian
1241 period. Our model further shows that the westward deflection of the Cenomanian-Turonian
1242 sandy submarine fan is a result of increasing differential tectonic subsidence from eastern to
1243 western GoM and may extend further west. Our study establishes a robust framework for
1244 understanding the complex tectonic history of the GoM and provides valuable insights that lay
1245 the groundwork for future research on the evolution of passive rift margins worldwide.

1246
1247

1248 **Acknowledgements**

1249

1250 This project received support from BHP through the STELLAR industry collaboration. SZ was
1251 supported by Australian Research Council grant DE210100084 and MS by DP200100966.
1252 pyGPlates and GPlates development is funded by the AuScope National Collaborative Research
1253 Infrastructure System (NCRIS) program.

1254

1255 **Open Research**

1256 The model was created by open source software GPlates (<https://www.gplates.org>) and python
1257 library pyGPlates. All the figures are generated using matplotlib library (<https://matplotlib.org/>)
1258 Reconstruction model files and workflows available from [10.5281/zenodo.10165818](https://doi.org/10.5281/zenodo.10165818)

1259

1260

1261 **References**

1262

1263 Adams, R. L. (2007). Basement Tectonics and the Origin of the Sabine Uplift. *Houston*
1264 *Geological Society Bulletin*, 49(9), 19–19.

1265 Anderson, T. H., & Schmidt, V. A. (1983). The evolution of Middle America and the Gulf of
1266 Mexico–Caribbean Sea region during Mesozoic time. *Geological Society of America*

- 1267 *Bulletin*, 94(8), 941. <https://doi.org/10.1130/0016->
1268 7606(1983)94<941:TEOMAA>2.0.CO;2
- 1269 Armitage, J. J., Collier, J. S., & Minshull, T. A. (2010). The importance of rift history for
1270 volcanic margin formation. *Nature*, 465(7300), 913–917.
1271 <https://doi.org/10.1038/nature09063>
- 1272 Bonatti, E. (1985). Punctiform initiation of seafloor spreading in the Red Sea during transition
1273 from a continental to an oceanic rift. *Nature*, 316(6023), 33–37.
1274 <https://doi.org/10.1038/316033a0>
- 1275 Boschman, L. M., van Hinsbergen, D. J. J., Torsvik, T. H., Spakman, W., & Pindell, J. L. (2014).
1276 Kinematic reconstruction of the Caribbean region since the Early Jurassic. *Earth-Science*
1277 *Reviews*, 138, 102–136. <https://doi.org/10.1016/j.earscirev.2014.08.007>
- 1278 Bott, M. H. P. (1992). The stress regime associated with continental break-up. *Geological*
1279 *Society, London, Special Publications*, 68(1), 125–136.
1280 <https://doi.org/10.1144/GSL.SP.1992.068.01.08>
- 1281 Brune, S., Heine, C., Clift, P. D., & Pérez-Gussinyé, M. (2017). Rifted margin architecture and
1282 crustal rheology: Reviewing Iberia-Newfoundland, Central South Atlantic, and South
1283 China Sea. *Marine and Petroleum Geology*, 79, 257–281.
1284 <https://doi.org/10.1016/j.marpetgeo.2016.10.018>
- 1285 Brune, S., Kolawole, F., Olive, J.-A., Stamps, D. S., Buck, W. R., Buitert, S. J. H., et al. (2023).
1286 Geodynamics of continental rift initiation and evolution. *Nature Reviews Earth &*
1287 *Environment*, 1–19. <https://doi.org/10.1038/s43017-023-00391-3>
- 1288 Cannat, M., Sauter, D., Bezos, A., Meyzen, C., Humler, E., & Le Rigoleur, M. (2008). Spreading
1289 rate, spreading obliquity, and melt supply at the ultraslow spreading Southwest Indian

- 1290 Ridge. *Geochemistry, Geophysics, Geosystems*, 9(4).
1291 <https://doi.org/10.1029/2007GC001676>
- 1292 Chenin, P., Schmalholz, S. M., Manatschal, G., & Karner, G. D. (2018). Necking of the
1293 Lithosphere: A Reappraisal of Basic Concepts With Thermo-Mechanical Numerical
1294 Modeling. *Journal of Geophysical Research: Solid Earth*, 123(6), 5279–5299.
1295 <https://doi.org/10.1029/2017JB014155>
- 1296 Christeson, G. L., Van Avendonk, H. J. A., Norton, I. O., Snedden, J. W., Eddy, D. R., Karner, G.
1297 D., & Johnson, C. A. (2014). Deep crustal structure in the eastern Gulf of Mexico.
1298 *Journal of Geophysical Research: Solid Earth*, 119(9), 6782–6801.
1299 <https://doi.org/10.1002/2014JB011045>
- 1300 Chu, D., & Gordon, R. G. (1998). Current plate motions across the Red Sea. *Geophysical*
1301 *Journal International*, 135(2), 313–328. [https://doi.org/10.1046/j.1365-](https://doi.org/10.1046/j.1365-246X.1998.00658.x)
1302 [246X.1998.00658.x](https://doi.org/10.1046/j.1365-246X.1998.00658.x)
- 1303 Colletta, B., Le Quellec, P., Letouzey, J., & Moretti, I. (1988). Longitudinal evolution of the Suez
1304 rift structure (Egypt). *Tectonophysics*, 153(1), 221–233. [https://doi.org/10.1016/0040-](https://doi.org/10.1016/0040-1951(88)90017-0)
1305 [1951\(88\)90017-0](https://doi.org/10.1016/0040-1951(88)90017-0)
- 1306 Davison, I., Anderson, L., & Nuttall, P. (2012). Salt deposition, loading and gravity drainage in
1307 the Campos and Santos salt basins. *Geological Society of London Special Publications*,
1308 363, 159–174. <https://doi.org/10.1144/SP363.8>
- 1309 Dickinson, W. R., Gehrels, G. E., & Stern, R. J. (2010). Late Triassic Texas uplift preceding
1310 Jurassic opening of the Gulf of Mexico: Evidence from U-Pb ages of detrital zircons.
1311 *Geosphere*, 6(5), 641–662. <https://doi.org/10.1130/GES00532.1>

- 1312 Ebinger, C. J., Keir, D., Bastow, I. D., Whaler, K., Hammond, J. O. S., Ayele, A., et al. (2017).
1313 Crustal Structure of Active Deformation Zones in Africa: Implications for Global Crustal
1314 Processes. *Tectonics*, 36(12), 3298–3332. <https://doi.org/10.1002/2017TC004526>
- 1315 Eddy, D. R., Van Avendonk, H. J. A., Christeson, G. L., Norton, I. O., Karner, G. D., Johnson, C.
1316 A., & Snedden, J. W. (2014). Deep crustal structure of the northeastern Gulf of Mexico:
1317 Implications for rift evolution and seafloor spreading. *Journal of Geophysical Research:*
1318 *Solid Earth*, 119(9), 6802–6822. <https://doi.org/10.1002/2014JB011311>
- 1319 Eddy, D. R., Van Avendonk, H. J. A., Christeson, G. L., & Norton, I. O. (2018). Structure and
1320 origin of the rifted margin of the northern Gulf of Mexico. *Geosphere*, 14(4), 1804–1817.
1321 <https://doi.org/10.1130/GES01662.1>
- 1322 Escalona, A., Norton, I. O., Lawver, L. A., & Gahagan, L. (2021). Quantitative Plate Tectonic
1323 Reconstructions of the Caribbean Region from Jurassic to Present. *Memoir 123: South*
1324 *America-Caribbean-Central Atlantic Plate Boundary, 2021*, 239–263.
1325 <https://doi.org/10.1306/13692247M1233849>
- 1326 Fiduk, J., Weimer, P., Trudgill, B., & Rowan, M. (1999). The Perdido Fold Belt, Northwestern
1327 Deep Gulf of Mexico, Part 2: Seismic Stratigraphy and Petroleum Systems1. *AAPG*
1328 *Bulletin*, 83.
- 1329 Filina, I. (2019). Crustal architecture of the northwestern and central Gulf of Mexico from
1330 integrated geophysical analysis. *Interpretation*, 7(4), T899–T910.
1331 <https://doi.org/10.1190/INT-2018-0258.1>
- 1332 Filina, I., & Beutel, E. (2022). *Geological and Geophysical Constraints Guide New Tectonic*
1333 *Reconstruction of the Gulf of Mexico*. <https://doi.org/10.1002/essoar.10511463.1>

- 1334 Filina, I., & Hartford, L. (2021). Subsurface structures along western Yucatan from integrated
1335 geophysical analysis. *Marine and Petroleum Geology*, *127*, 104964.
1336 <https://doi.org/10.1016/j.marpetgeo.2021.104964>
- 1337 Filina, I., Austin, J., Doré, T., Johnson, E., Minguez, D., Norton, I., et al. (2022). Opening of the
1338 Gulf of Mexico: What we know, what questions remain, and how we might answer them.
1339 *Tectonophysics*, *822*, 229150. <https://doi.org/10.1016/j.tecto.2021.229150>
- 1340 Freeland, G. L., & Dietz, R. S. (1971). Plate Tectonic Evolution of Caribbean–Gulf of Mexico
1341 Region. *Nature*, *232*(5305), 20–23. <https://doi.org/10.1038/232020a0>
- 1342 Funck, T., Geissler, W. H., Kimbell, G. S., Gradmann, S., Erlendsson, Ö., McDermott, K., &
1343 Petersen, U. K. (2017). Moho and basement depth in the NE Atlantic Ocean based on
1344 seismic refraction data and receiver functions. *Geological Society, London, Special*
1345 *Publications*, *447*(1), 207–231. <https://doi.org/10.1144/SP447.1>
- 1346 Gurnis, M., Yang, T., Cannon, J., Turner, M., Williams, S., Flament, N., & Müller, R. D. (2018).
1347 Global tectonic reconstructions with continuously deforming and evolving rigid plates.
1348 *Computers & Geosciences*, *116*, 32–41. <https://doi.org/10.1016/j.cageo.2018.04.007>
- 1349 Gustafson, L. B., & Williams, N. (1981). Sediment-Hosted Stratiform Deposits of Copper, Lead,
1350 and Zinc. In B. J. Skinner (Ed.), *Seventy-Fifth Anniversary Volume* (p. 0). Society of
1351 Economic Geologists. <https://doi.org/10.5382/AV75.06>
- 1352 Harry, D. L., Londono, J., & Huerta, A. (2003). Early Paleozoic transform-margin structure
1353 beneath the Mississippi coastal plain, southeast United States. *Geology*, *31*(11), 969–972.
1354 <https://doi.org/10.1130/G19787.1>
- 1355 Hitzman, M., Kirkham, R., Broughton, D., Thorson, J., & Selley, D. (2005). The Sediment-
1356 Hosted Stratiform Copper Ore System. In J. W. Hedenquist, J. F. H. Thompson, R. J.

- 1357 Goldfarb, & J. P. Richards (Eds.), *One Hundredth Anniversary Volume* (p. 0). Society of
1358 Economic Geologists. <https://doi.org/10.5382/AV100.19>
- 1359 Horn, B. W., Goswami, A., Haire, E., Radovich, B., McGrail, A., & Pindell, J. (2016). Extended
1360 Abstract: Regional Interpretation Across the Entire Gulf of Mexico Basin – A New
1361 Perspective. *The Houston Geological Society Bulletin*, 58(7), 31–33. Retrieved from
1362 http://archives.datapages.com/data/HGS/vol58/058007/31_hgs580031.htm
- 1363 Hosseinpour, M., Müller, D., Williams, S., & Whittaker, J. (2013). Full-fit reconstruction of the
1364 Labrador Sea and Baffin Bay. *Solid Earth*, 4, 461–479. [https://doi.org/10.5194/se-4-461-](https://doi.org/10.5194/se-4-461-2013)
1365 2013
- 1366 Hudec, M. R., Norton, I. O., Jackson, M. P. A., & Peel, F. J. (2013). Jurassic evolution of the
1367 Gulf of Mexico salt basin. *AAPG Bulletin*, 97(10), 1683–1710.
1368 <https://doi.org/10.1306/04011312073>
- 1369 Hudec, M. R., Dooley, T. P., Peel, F. J., & Soto, J. I. (2019). Controls on the evolution of passive-
1370 margin salt basins: Structure and evolution of the Salina del Bravo region, northeastern
1371 Mexico. *GSA Bulletin*, 132(5–6), 997–1012. <https://doi.org/10.1130/B35283.1>
- 1372 Huerta, A. D., & Harry, D. L. (2012). Wilson cycles, tectonic inheritance, and rifting of the North
1373 American Gulf of Mexico continental margin. *Geosphere*, 8(2), 374–385.
1374 <https://doi.org/10.1130/GES00725.1>
- 1375 Izquierdo-Llavall, E., Ringenbach, J. C., Sapin, F., Rives, T., & Callot, J. P. (2022). Crustal
1376 structure and lateral variations in the Gulf of Mexico conjugate margins: From rifting to
1377 break-up. *Marine and Petroleum Geology*, 136, 105484.
1378 <https://doi.org/10.1016/j.marpetgeo.2021.105484>

- 1379 James, P., Ernesto, M. C., Alejandro, C., & Leopoldo, H. (2016). Aeromagnetic Map Constrains
1380 Jurassic-Early Cretaceous Synrift, Break Up, and Rotational Seafloor Spreading History
1381 in the Gulf of Mexico. In C. M. Lowery, J. W. Snedden, & N. C. Rosen (Eds.), *Mesozoic*
1382 *of the Gulf Rim and Beyond: New Progress in Science and Exploration of the Gulf of*
1383 *Mexico Basin* (Vol. 35, p. 0). SEPM Society for Sedimentary Geology.
1384 <https://doi.org/10.5724/gcs.15.35.0123>
- 1385 Jarvis, G. T., & McKenzie, D. P. (1980). Sedimentary basin formation with finite extension rates.
1386 *Earth and Planetary Science Letters*, 48(1), 42–52. [https://doi.org/10.1016/0012-](https://doi.org/10.1016/0012-821X(80)90168-5)
1387 [821X\(80\)90168-5](https://doi.org/10.1016/0012-821X(80)90168-5)
- 1388 Kaban, M. K., Tesauro, M., Mooney, W. D., & Cloetingh, S. A. P. L. (2014). Density,
1389 temperature, and composition of the North American lithosphere—New insights from a
1390 joint analysis of seismic, gravity, and mineral physics data: 1. Density structure of the
1391 crust and upper mantle. *Geochemistry, Geophysics, Geosystems*, 15(12), 4781–4807.
1392 <https://doi.org/10.1002/2014GC005483>
- 1393 Kelemen, P. B., & Holbrook, W. S. (1995). Origin of thick, high-velocity igneous crust along the
1394 U.S. East Coast Margin. *Journal of Geophysical Research: Solid Earth*, 100(B6), 10077–
1395 10094. <https://doi.org/10.1029/95JB00924>
- 1396 Kneller, E. A., & Johnson, C. A. (2011). Plate Kinematics of the Gulf of Mexico Based on
1397 Integrated Observations from the Central and South Atlantic. *Gulf Coast Association of*
1398 *Geological Societies Transactions*, 283–300. Retrieved from
1399 http://archives.datapages.com/data/gcags/data/061/061001/283_gcags610283.htm

- 1400 Le Pichon, X., & Sibuet, J.-C. (1981). Passive margins: A model of formation. *Journal of*
1401 *Geophysical Research: Solid Earth*, 86(B5), 3708–3720.
1402 <https://doi.org/10.1029/JB086iB05p03708>
- 1403 Lundin, E.R., & Doré, A. G. (2017). The Gulf of Mexico and Canada Basin: Genetic Siblings on
1404 Either Side of North America. *GSA Today*, 4–11. <https://doi.org/10.1130/GSATG274A.1>
- 1405 Lundin, Erik R., Redfield, T. F., & Péron-Pindivic, G. (2014). Rifted Continental Margins:
1406 Geometric Influence on Crustal Architecture and Melting. In James Pindell, B. Horn, N.
1407 Rosen, P. Weimer, M. Dinkleman, A. Lowrie, et al. (Eds.), *Sedimentary Basins: Origin,*
1408 *Depositional Histories, and Petroleum Systems* (Vol. 33, p. 0). SEPM Society for
1409 Sedimentary Geology. <https://doi.org/10.5724/gcs.14.33.0018>
- 1410 Maldonado, R., Weber, B., Ortega-Gutiérrez, F., & Solari, L. A. (2018). High-pressure
1411 metamorphic evolution of eclogite and associated metapelite from the Chuacús complex
1412 (Guatemala Suture Zone): Constraints from phase equilibria modelling coupled with Lu-
1413 Hf and U-Pb geochronology. *Journal of Metamorphic Geology*, 36(1), 95–124.
1414 <https://doi.org/10.1111/jmg.12285>
- 1415 Mark V. Shann, K. V.-R., & Horbury, A. D. (2020). The Sureste Super Basin of southern Mexico.
1416 *AAPG Bulletin*, 104(12), 2643–2700. <https://doi.org/10.1306/09172020081>
- 1417 Marton, G., & Buffler, R. T. (1994). Jurassic Reconstruction of the Gulf of Mexico Basin.
1418 *International Geology Review*, 36(6), 545–586.
1419 <https://doi.org/10.1080/00206819409465475>
- 1420 Marzoli, A., Callegaro, S., Dal Corso, J., Davies, J. H. F. L., Chiaradia, M., Youbi, N., et al.
1421 (2018). The Central Atlantic Magmatic Province (CAMP): A Review. In L. H. Tanner

- 1422 (Ed.), *The Late Triassic World: Earth in a Time of Transition* (pp. 91–125). Cham:
1423 Springer International Publishing. https://doi.org/10.1007/978-3-319-68009-5_4
- 1424 McKenzie, D. (1978). Some remarks on the development of sedimentary basins. *Earth and*
1425 *Planetary Science Letters*, 40(1), 25–32. [https://doi.org/10.1016/0012-821X\(78\)90071-7](https://doi.org/10.1016/0012-821X(78)90071-7)
- 1426 Meyer, B., Saltus, R., & Chulliat, A. (2017). EMAG2v3: Earth Magnetic Anomaly Grid (2-arc-
1427 minute resolution) *NOAA National Centers for Environmental Information*.
1428 <https://doi.org/10.7289/V5H70CVX>. Retrieved July 21, 2023, from
1429 <https://doi.org/10.7289/V5H70CVX>
- 1430 Michael R. Hudec, & Norton, I. O. (2019). Upper Jurassic structure and evolution of the Yucatán
1431 and Campeche subbasins, southern Gulf of Mexico. *AAPG Bulletin*, 103(5), 1133–1151.
1432 <https://doi.org/10.1306/11151817405>
- 1433 Milliken, J. V. (1988). *Late Paleozoic and Early Mesozoic geologic evolution of the Arklatex*
1434 *Area* (Master's Thesis). Rice University. <https://hdl.handle.net/1911/13309>
- 1435 Minguetz, D., Gerald Hensel, E., & Johnson, E. A. E. (2020). A fresh look at Gulf of Mexico
1436 tectonics: Testing rotations and breakup mechanisms from the perspective of seismically
1437 constrained potential-fields modeling and plate kinematics. *Interpretation*, 8(4), SS31–
1438 SS45. <https://doi.org/10.1190/INT-2019-0256.1>
- 1439 Montaron, B., & Tapponnier, P. (2009). *A quantitative model for salt deposition in actively*
1440 *spreading basins*. Search and Discovery Article
1441 <https://doi.org/10.13140/RG.2.1.4078.8000>
- 1442 Müller, R. D., Seton, M., Zahirovic, S., Williams, S. E., Matthews, K. J., Wright, N. M., et al.
1443 (2016). Ocean basin evolution and global-scale plate reorganization events since Pangea
1444 breakup. *Annual Review of Earth and Planetary Sciences*, 44(1), 107–138.

- 1445 Müller, R. D., Zahirovic, S., Williams, S. E., Cannon, J., Seton, M., Bower, D. J., et al. (2019). A
1446 Global Plate Model Including Lithospheric Deformation Along Major Rifts and Orogens
1447 Since the Triassic. *Tectonics*, 38(6), 1884–1907. <https://doi.org/10.1029/2018TC005462>
- 1448 Naliboff, J., & Buiter, S. J. H. (2015). Rift reactivation and migration during multiphase
1449 extension. *Earth and Planetary Science Letters*, 421, 58–67.
1450 <https://doi.org/10.1016/j.epsl.2015.03.050>
- 1451 Nemčok, M. (Ed.). (2016). Determination of unstretched continental, thinned continental, proto-
1452 oceanic, and oceanic crustal boundaries. In *Rifts and Passive Margins: Structural*
1453 *Architecture, Thermal Regimes, and Petroleum Systems* (pp. 76–96). Cambridge:
1454 Cambridge University Press. <https://doi.org/10.1017/CBO9781139198844.004>
- 1455 Nicholas, R. L., & Waddell, D. E. (1989). The Ouachita system in the subsurface of Texas,
1456 Arkansas, and Louisiana. In R. D. Hatcher Jr., W. A. Thomas, & G. W. Viele (Eds.), *The*
1457 *Appalachian-Ouachita Orogen in the United States* (Vol. F-2, p. 0). Geological Society of
1458 America. <https://doi.org/10.1130/DNAG-GNA-F2.661>
- 1459 O'Reilly, C., Keay, J., Birch-Hawkins, A., Bate, D., Halliday, J., & TGS. (2017). Regional Play
1460 Types in the Mexican Offshore. *GEO ExPro Magazine*. Retrieved from
1461 <https://archives.datapages.com/data/geo-expro-magazine/014/014004/pdfs/36.html>
- 1462 Pilcher, R. S., Murphy, R. T., & McDonough Ciosek, J. (2014). Jurassic raft tectonics in the
1463 northeastern Gulf of Mexico. *Interpretation*, 2(4), SM39–SM55.
1464 <https://doi.org/10.1190/INT-2014-0058.1>
- 1465 Pindell, J., Graham, R., & Horn, B. (2014). Rapid outer marginal collapse at the rift to drift
1466 transition of passive margin evolution, with a Gulf of Mexico case study. *Basin Research*,
1467 26(6), 701–725. <https://doi.org/10.1111/bre.12059>

- 1468 Pindell, J. L. (1985). Alleghenian reconstruction and subsequent evolution of the Gulf of Mexico,
1469 Bahamas, and Proto-Caribbean. *Tectonics*, 4(1), 1–39.
1470 <https://doi.org/10.1029/TC004i001p00001>
- 1471 Pindell, James, Villagómez, D., Molina-Garza, R., Graham, R., & Weber, B. (2021). A revised
1472 synthesis of the rift and drift history of the Gulf of Mexico and surrounding regions in the
1473 light of improved age dating of the Middle Jurassic salt. *Geological Society, London,*
1474 *Special Publications*, 504(1), 29–76. <https://doi.org/10.1144/SP504-2020-43>
- 1475 Pindell, Jim, & Kennan, L. (2009). Tectonic evolution of the Gulf of Mexico, Caribbean and
1476 northern South America in the mantle reference frame: An update. *Geological Society,*
1477 *London, Special Publications*, 328, 1–55. <https://doi.org/10.1144/SP328.1>
- 1478 Reguzzoni, M., & Sampietro, D. (2015). GEMMA: An Earth crustal model based on GOCE
1479 satellite data. *International Journal of Applied Earth Observation and Geoinformation*,
1480 35, 31–43. <https://doi.org/10.1016/j.jag.2014.04.002>
- 1481 Rowan, M. G. (2014). Passive-margin salt basins: hyperextension, evaporite deposition, and salt
1482 tectonics. *Basin Research*, 26(1), 154–182. <https://doi.org/10.1111/bre.12043>
- 1483 Rubio-Cisneros, I. I., & Lawton, T. F. (2011). Detrital zircon U-Pb ages of sandstones in
1484 continental red beds at Valle de Huizachal, Tamaulipas, NE Mexico: Record of Early-
1485 Middle Jurassic arc volcanism and transition to crustal extension. *Geosphere*, 7(1), 159–
1486 170. <https://doi.org/10.1130/GES00567.1>
- 1487 Salvador, A. (1991). Origin and development of the Gulf of Mexico basin. In A. Salvador (Ed.),
1488 *The Gulf of Mexico Basin* (Vol. J, p. 0). Geological Society of America.
1489 <https://doi.org/10.1130/DNAG-GNA-J.389>

- 1490 Sandwell, D. T., Harper, H., Tozer, B., & Smith, W. H. F. (2021). Gravity field recovery from
1491 geodetic altimeter missions. *Advances in Space Research*, 68(2), 1059–1072.
1492 <https://doi.org/10.1016/j.asr.2019.09.011>
- 1493 Sawkins, F. J. (1990). Metal Deposits and Plate Tectonics — An Attempt at Perspective. In F. J.
1494 Sawkins (Ed.), *Metal Deposits in Relation to Plate Tectonics* (pp. 377–388). Berlin,
1495 Heidelberg: Springer. https://doi.org/10.1007/978-3-662-08681-0_11
- 1496 Scott, K. R., Hayes, W. E., & Fietz, R. P. (1961). Geology of the Eagle Mills Formation, *II*.
1497 Retrieved from <http://archives.datapages.com/data/gcags/data/011/011001/0001.htm>
- 1498 Şengör, A. M. C., & Natal'in, B. A. (2001). Rifts of the world. In R. E. Ernst & K. L. Buchan
1499 (Eds.), *Mantle plumes: their identification through time* (Vol. 352, p. 0). Geological
1500 Society of America. <https://doi.org/10.1130/0-8137-2352-3.389>
- 1501 Seton, M., Müller, R. D., Zahirovic, S., Gaina, C., Torsvik, T., Shephard, G., et al. (2012). Global
1502 continental and ocean basin reconstructions since 200Ma. *Earth-Science Reviews*, 113(3),
1503 212–270. <https://doi.org/10.1016/j.earscirev.2012.03.002>
- 1504 Snedden, J., Virdell, J., Whiteaker, T., & Ganey-Curry, P. (2016). A basin-scale perspective on
1505 Cenomanian-Turonian (Cretaceous) depositional systems, greater Gulf of Mexico (USA).
1506 *Interpretation*, 4, SC1–SC22. <https://doi.org/10.1190/INT-2015-0082.1>
- 1507 Snedden, J. W., & Galloway, W. E. (2019). *The Gulf of Mexico Sedimentary Basin: Depositional*
1508 *Evolution and Petroleum Applications*. Cambridge: Cambridge University Press.
1509 <https://doi.org/10.1017/9781108292795>
- 1510 Snedden, J. W., Norton, I., Hudec, M., Eljalafi, A., & Peel, F. (2018). Paleogeographic
1511 Reconstruction of the Louann Salt Basin in the Gulf of Mexico. Presented at the AAPG
1512 Annual Convention and Exhibition, Salt Lake City, Utah. Retrieved from

1513 <https://www.searchanddiscovery.com/abstracts/html/2018/ace2018/abstracts/2855365.htm>
1514 ml

1515 Steier, A., & Mann, P. (2019). Late Mesozoic gravity sliding and Oxfordian hydrocarbon
1516 reservoir potential of the northern Yucatan margin. *Marine and Petroleum Geology*, *103*,
1517 681–701. <https://doi.org/10.1016/j.marpetgeo.2019.03.001>

1518 Tetreault, J. L., & Buiters, S. J. H. (2018). The influence of extension rate and crustal rheology on
1519 the evolution of passive margins from rifting to break-up. *Tectonophysics*, *746*, 155–172.
1520 <https://doi.org/10.1016/j.tecto.2017.08.029>

1521 Tugend, J., Gillard, M., Manatschal, G., Nirrengarten, M., Harkin, C., Epin, M.-E., et al. (2020).
1522 Reappraisal of the magma-rich versus magma-poor rifted margin archetypes. *Geological*
1523 *Society, London, Special Publications*, *476*(1), 23–47. <https://doi.org/10.1144/SP476.9>

1524 Umbarger, K. F. (2018, December 31). *Late Triassic North American Paleodrainage Networks*
1525 *and Sediment Dispersal of the Chinle Formation: A Quantitative Approach Utilizing*
1526 *Detrital Zircons* (Thesis). University of Kansas. Retrieved from
1527 <https://kuscholarworks.ku.edu/handle/1808/27833>

1528 Van Avendonk, H., Christeson, G., Norton, I., & Eddy, D. (2015). Continental rifting and
1529 sediment infill in the northwestern Gulf of Mexico. *Geology*, *43*.
1530 <https://doi.org/10.1130/G36798.1>

1531 Warren, J. K. (2006). *Evaporites: Sediments, Resources and Hydrocarbons*. Springer Science &
1532 Business Media. <https://doi.org/10.1007/3-540-32344-9>

1533 White, R., & McKenzie, D. (1989). Magmatism at rift zones: The generation of volcanic
1534 continental margins and flood basalts. *Journal of Geophysical Research: Solid Earth*,
1535 *94*(B6), 7685–7729. <https://doi.org/10.1029/JB094iB06p07685>

- 1536 Wiley, K. S. (2017). Provenance of Syn-rift Clastics in the Eastern Gulf of Mexico: Insight from
1537 U-Pb Detrital Zircon Geochronology and Thin Sections. *Graduate Theses, Dissertations,*
1538 *and Problem Reports*. <https://doi.org/10.33915/etd.6951>
- 1539 Williams-Rojas, C. T., Reyes-Tovar, E., Miranda-Peralta, L., Reyna-Martinez, G., Cardenas-
1540 Alvarado, A., Maldonado-Villalon, R., et al. (2012). Extended Abstract: Hydrocarbon
1541 Potential of the Deepwater Portion of the “Salina del Istmo” Province, Southeastern Gulf
1542 of Mexico, Mexico. *Gulf Coast Association of Geological Societies Transactions*. 641–
1543 644. Retrieved from
1544 http://archives.datapages.com/data/gcags/data/062/062001/641_gcags620641.htm
- 1545
1546
1547
1548
1549